Annual Report

DETECTION AND CLASSIFICATION

OF BURIED METALLIC OBJECTS

UX-1225

Lawrence Berkeley National Laboratory

January 2003

p.o.c.: LBL, 1 Cyclotron Road, MS:90-1116, Berkeley, CA 94720.
E-mail: EGasperikova@lbl.gov

TABLE OF CONTENTS

1. INTRODUCTION

1.1 Background

In the search for UXO and for discrimination between UXO and non-UXO metallic fragments (clutter) a prime requirement is to determine accurately the response parameters that characterize a metallic object in the ground. A search system is needed that not only detects the object but that can determine the size, shape, orientation, shell thickness and metal content (ferrous or non-ferrous, mixed metals). The latter properties of a buried metallic object are referred to here as the parameters of the object.

The search for UXO is a two step process. The object must first be detected and its location determined. This is now accomplished with a variety of magnetometer and active electromagnetic (AEM) systems. The AEM systems operate in the transient or frequency domain mode and usually with a single transmitter and single receiver. The characterization step requires that a variety of incident fields be used to stimulate induced magnetization and induced current flow in different directions within the object. The secondary fields from these induced magnetizations are then used to determine the parameters of the object. This more detailed second step requires the broadband spectral or transient response using frequencies low enough to identify the quasi dc magnetization response and high enough to identify the purely electromagnetic (EM), inductive limit, response which depends only on the size of the object.

Optimum in this report means an EM system that can extract from the measurements the best possible estimates of the location, orientation, size, shape and metal content of a buried metallic object in the presence of the interfering response of the ground and non-UXO metallic objects. Discrimination can be achieved partly by selective filtering of the responses inherent in the system configuration and design and partly through post acquisition processing. The parameters of the target will be obtained by a statistical inversion of the measurements to establish the principal electromagnetic moments of the detected object.

1.2 Objectives

In summary the technical objectives of this project are:

1) To develop and demonstrate a methodology for quantitative evaluation of existing AEM systems and for the design of new systems.

2) To implement a new methodology for optimizing an AEM system for detecting and classifying UXO of a given class in a specified geologic setting and in a given noise environment.

3) To design and build a prototype of an optimal active EM system for detecting and characterizing a metallic object in the ground.

1.3 Technical Approach

The design methodology is based on the use of simulators, numerical models of the electromagnetic response of an arbitrary target in the ground to an arbitrary configuration of transmitters and receivers. The variables in the simulator are the parameters of the targets, the parameters of the AEM system and the noise (ambient, motion, instrumental, and geologic). The target parameters are the location, orientation, depth, size, shape, metal content and type. A schematic of the simulator is shown in Figure 1.3.1.
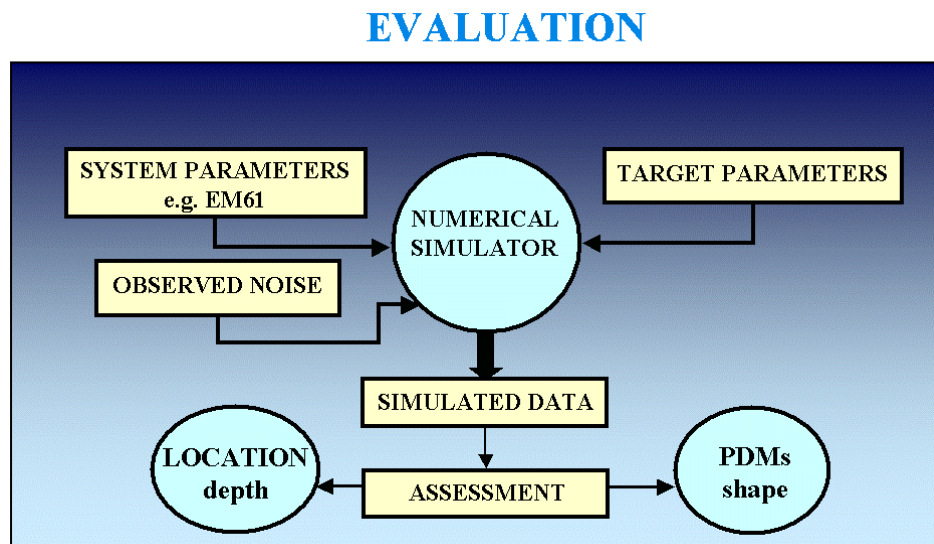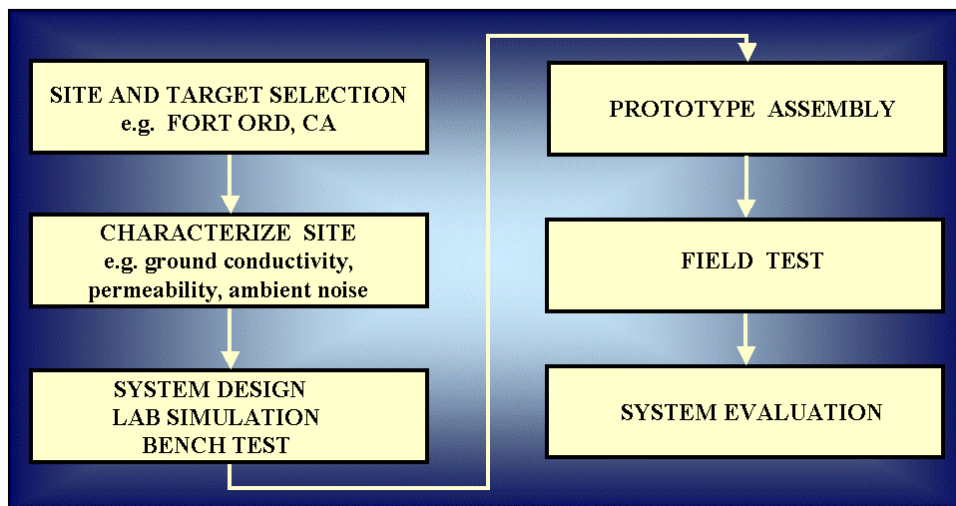

Figure 1.3.1 Schematic diagram of the simulator.

OPTIMIZATION
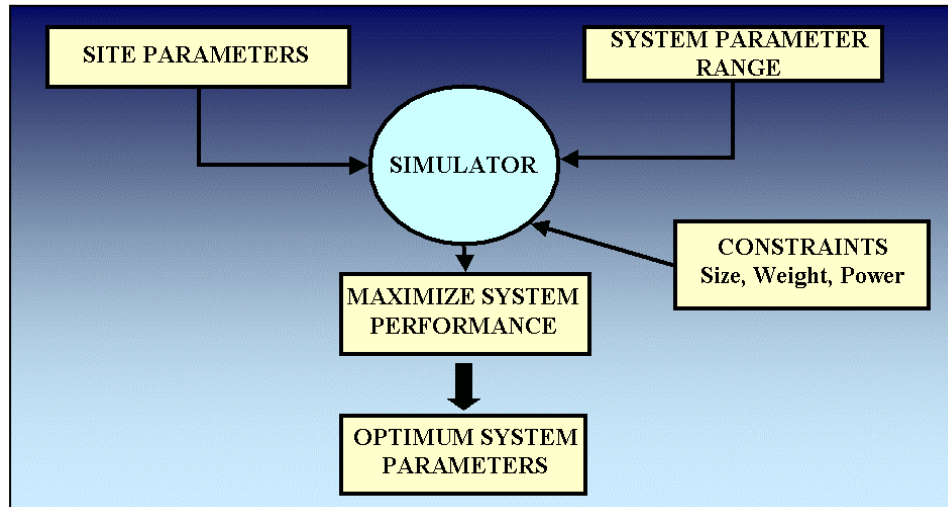
Figure 1.3.2 Schematic diagram of the optimization process.

VERIFICATION

Figure 1.3.3 Schematic diagram of the verification process.

The simulator can be used to evaluate designs by simulating the response of a given system, with a given noise level, to a particular target. Various system configurations can

5

be quantitatively compared through their respective signal to noise ratios over the same target.

This forward modeling approach is useful for evaluating the relative response of different targets for a given system, for example in analyzing the role of loop size in discriminating between small, shallow, targets and deeper, larger, ones. It is also useful for evaluating the ground response and modeling the spectral or transient response of various targets

The system parameters that are variables in the design are: a) the geometric configuration of the transmitter(s) and receivers(s) and the way in which they are mounted for given target objectives (the platform), b) the spatial positioning of the system (profile, grid, single site stand-off, etc.), c) the transmitter power and waveform, d) the system and ambient noise, e) the receiver bandwidth and dynamic range, f) the signal averaging time (a function of survey speed). The geologic variables (geologic noise) are the values and variability of the ground conductivity and permeability. A more detailed schematic of all the variables that contribute to the data acquired with a general AEM system is shown in Figure 1.3.4.
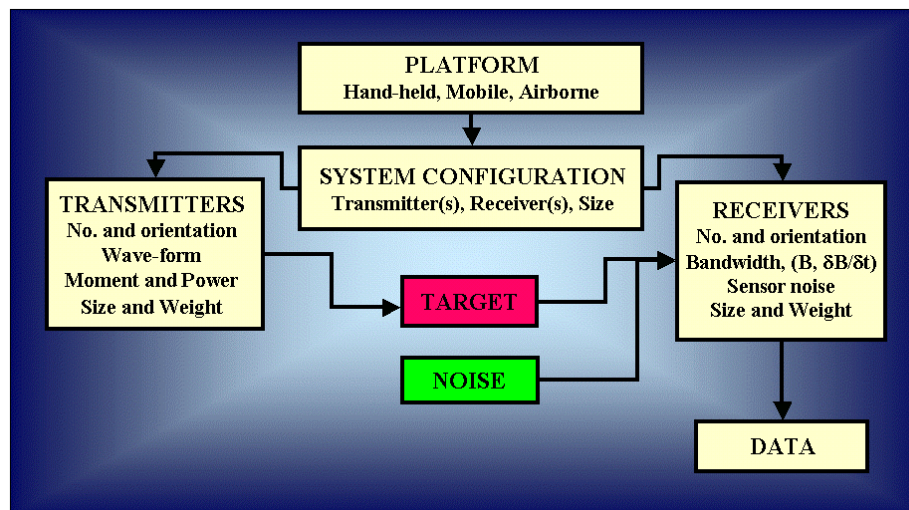
Figure 1.3.4 Generic AEM System.

## 2. PERFORMANCE ASSESSMENT AND DIRECT OPTIMIZATION

2.1 Introduction

The broad definition of optimum in this report is an active EM system that can extract, from the measurements, the best possible estimates of the location, orientation, depth, size, shape, and metal content of a buried metallic object in the presence of the interfering response of non-UXO metallic objects. Discrimination can be achieved partly through selective filtering of the response inherent in the system design and partly through post acquisition processing. These parameters are never determined perfectly because of a fundamental non-uniqueness in the solutions (the response of the target) to the governing equations. Also, practical limitations introduced by depth of the target, the response of a general, inhomogeneous, ground and the presence of response from other non-UXO metallic objects, as well as the signal to noise limitations imposed by weight and power considerations, introduce constraints on what is achievable. An optimum system is bounded by these theoretical and practical considerations and at the end represents a compromise that detects, discriminates and classifies to an agreed upon criterion or specification.

There have been several theoretical and numerical studies of target responses for the new UXO EM systems, none of which have addressed the issue of optimization. Laboratory, field and theoretical analyses of the frequency domain GEM-3 (e.g. Won et al., 1997) and of the EM-61 and its variants EM61HH, EM63, etc. (e.g. McNeill and Bosnar, 1996; Khadr et al., 1998; Ware, 2000) for a range of targets have demonstrated some of the detection/classification properties and potential of these systems. The studies focused on the response of a particular system to various targets but not on the broader issue of what system would perform best over the targets. Some of these systems rely on the frequency domain (spectral) or time domain transient signal characteristics to classify the target (e.g. Keiswetter et al., 1999; Barrow et al. 1996; or Ware, 2000). Others rely on both the spectral response and the variation of response with transmitted field polarization (e.g. Bell et al., 1998; Khadr et al., 1998; Pasion and Oldenburg, 2001; Snyder et al., 1999). A fundamental and critical technical comparison of time and frequency approaches has been tactfully avoided.

Our research in the past year has clearly shown the importance of using multiple polarizations of the incident magnetic field to stimulate the principal induced magnetic polarizations of the target. The second step in the identification/discrimination process is then to measure the resulting secondary fields at enough points in space to uniquely determine these principal polarizations – the inversion or interpretation process. [Fundamentally the incident magnetic field induces a circulating current in a confined conductor. This current produces a magnetic dipole moment, usually referred to as M. If this moment is normalized by the inducing magnetic field, the resulting quantity is called the magnetic polarization. We use both terms in this report.] Finally the characterization depends on recovering the broadband polarization response. We address these steps in the following sections of the report.

The concept of identifying an object through the measurement of secondary fields arising from induced magnetization and induced currents is illustrated in the following cartoon.
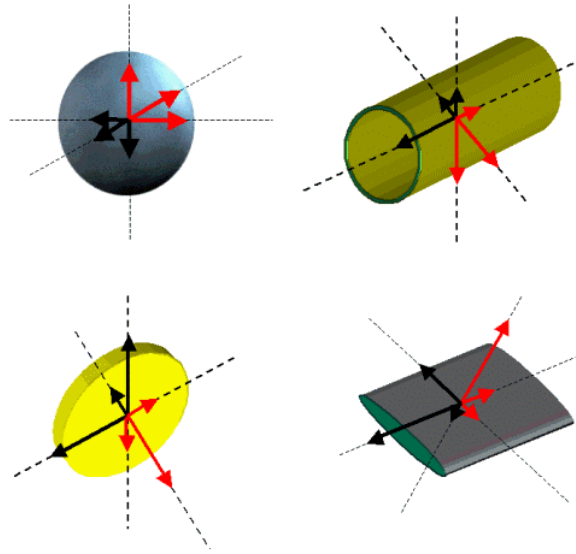
Figure 2.1.1

In any conducting permeable body placed in a magnetic field there are two types of induced magnetic moments. At zero frequency, dc, the incident magnetic field magnetizes the body so that it acquires a static magnetic dipole moment. This vector moment is in the direction of the inducing static magnetic field. As the frequency of the inducing field is increased a circulating current is induced to flow by virtue of Faraday's Law. This

circulating current produces a magnetic moment, which is in the opposite direction to the inducing magnetic field. The net magnetic moment, that is responsible for producing the so called secondary fields measured away from the body, is a function of the frequency, conductivity, permeability, size and shape of the body. In this cartoon the induced principal magnetic moments are shown in black and the induced principal electromagnetic moments, for a particular frequency, caused by the induced currents are shown in red. The characteristics of these principal moments, and how they change with frequency, are the basis of shape and metal content determination. The magnetic and EM moments are always in opposite directions. The sphere has equal moments in any three orthogonal directions. The disk and cylinder have two identical minor axis moments and a different axial moment, and the flattened ellipsoid has three different moments. It is also important to see from this cartoon that the magnetic moments behave differently from the EM moments and can be large in directions where the EM moments are small. For example in the thin disk the axial magnetization will be very small whereas the axial moment will be the largest for EM induction. [This simplistic description for the disk is in fact only valid for very thin disks. For a disk of appreciable thickness the coplanar EM moments can be quite large due to the increase in induction number caused by the permeability. A relative permeability of 200 effectively increases the thickness by 200 and consequently presents a large cross-sectional area to the inducing electromagnetic field.] These observations clearly illustrate the need for broadband coverage not only to separate ferrous from non-ferrous response but also to assist in relating the response to the shape of the body.

For regular bodies of revolution the induced moments are aligned with the symmetry axes of the object, and for a uniform inducing field they do not change direction with frequency. For an irregular object such as twisted scrap metal, the moment directions do change with frequency. For actual search systems the dimensions of the object may be comparable to the distance to, and size of, the transmitter and the moments may change size and direction as a function of frequency. In any event it is these induced moment characteristics that allow determination of the object parameters. To actually excite these moments it is clear that several polarizations of incident field are required.

A rigorous approach to the interpretation of the secondary fields measured with any particular search system would involve an inversion scheme to determine the parameters of

an object that best reproduced the field data in a numerical simulation of the actual system. Forward modeling codes for solid metallic objects of arbitrary shape are only now becoming available, and for bodies of arbitrary relative permeability and arbitrary frequency they are slow even on very fast computers. It is certainly impractical to consider this approach for real time processing and interpretation in the field. Further, there are at the moment no modeling codes for ferrous and non-ferrous shells of various shapes. Since these are needed to represent typical UXO (there being little interest in detecting solid iron cannon balls) another approach is needed to represent the response of metallic objects.

For purposes of design, system evaluation and interpretation we have adopted a simple *dipole* moment representation of a target. This is basically the same approach used by Khadr et al. (1998), Bell et al. (1998), Pasion and Oldenburg (2001) and Baum (1999). With this approximation it is assumed that any target can be represented by three orthogonal *dipole* moments, the principal dipole moments (PDM) or, if normalized by the incident field, the principal dipole polarizations (PDP). We have concluded from these studies and our own simulators that a satisfactory approach to characterizing the target is to recover the PDM's and their directions as a function of frequency or time. The use of PDM's greatly simplifies the inversion process used to find the location and vector PDM's of the object. Moreover this representation is a practical way to characterize any object since it basically encapsulates the response in a compact manner. A rigorous identification will require matching of the PDM's, as a function of frequency or time, to a catalogue of objects whose PDM's have been predetermined.

Smith and Morrison (2002) describe an inversion algorithm, which locates an object and recovers its PDM for a specific search system in a given amount of system noise. The inversion process inherently assigns uncertainties to the extracted target parameters and depth based on the uncertainties (noise) in the data. These uncertainties are the fundamental data used to assess the quality of the response and to estimate ROC curves. Smith et al. (2002) used this inversion algorithm to determine the depths of detection, to a given uncertainty, and PDM's to a given uncertainty, of simple target spheres for several search configurations. This inversion analysis underlies the design methodology described in this report.

2.2 Optimizing the transmitter-receiver configuration

The inversion algorithm described in Smith and Morrison (2002), and used for system comparison by Smith et al. (2002) is the fundamental tool used in this more generalized study. In a sense the approach used here can also be cast as an inverse problem: to determine the parameters of the AEM system that maximize the response for a given target subject to constraints on the system (size, platform, weight and power) and the anticipated ambient noise.

As with a rigorous inversion, the parameters of a proposed system are varied incrementally until a maximum response is obtained or until a maximum in signal to noise is obtained. For a given model and background, and with given system and ambient noise, the code is run repeatedly for changes in the system parameters until the variances in the estimated target parameters are minimized. This process provides an objective method for finding the optimum array configuration (i.e. the number of components and their spatial disposition, the transmitter moments and the bandwidth) needed to obtain the best estimate of the depth and vector principal moments of the target.

The first step in such a process can be seen in one of the examples shown in Smith et al. (2002) (Figure 2.2.1). Here uncertainty estimates are used to compute the depths to which the PDM's and dipole locations can be estimated for steel spheres of varying radius, for two transmitter-receiver configurations. One meter square transmitter loops were used with a moment of 180 Amp-m^2, and a receiver noise level of 1.97 nT/s in vertical field measurements, simulating an observed noise level, and 5.91 nT/s in horizontal field components (when present) simulating the larger noise levels observed in horizontal components. A step function turn-off transmitter current was used, as the most generic of waveforms, and an observation time of 610 μs after turnoff chosen to simulate the effective center time of the averaging gate of an existent commercial transmitter-receiver (T-R) system. For each radius sphere and for each T-R configuration the relative root mean squared (rms) inverted moment uncertainty and depth uncertainty were computed as a function of sphere depth, for spheres directly below the center of a 9 x 9 grid of system placements with 0.4 m spacing in x and y.
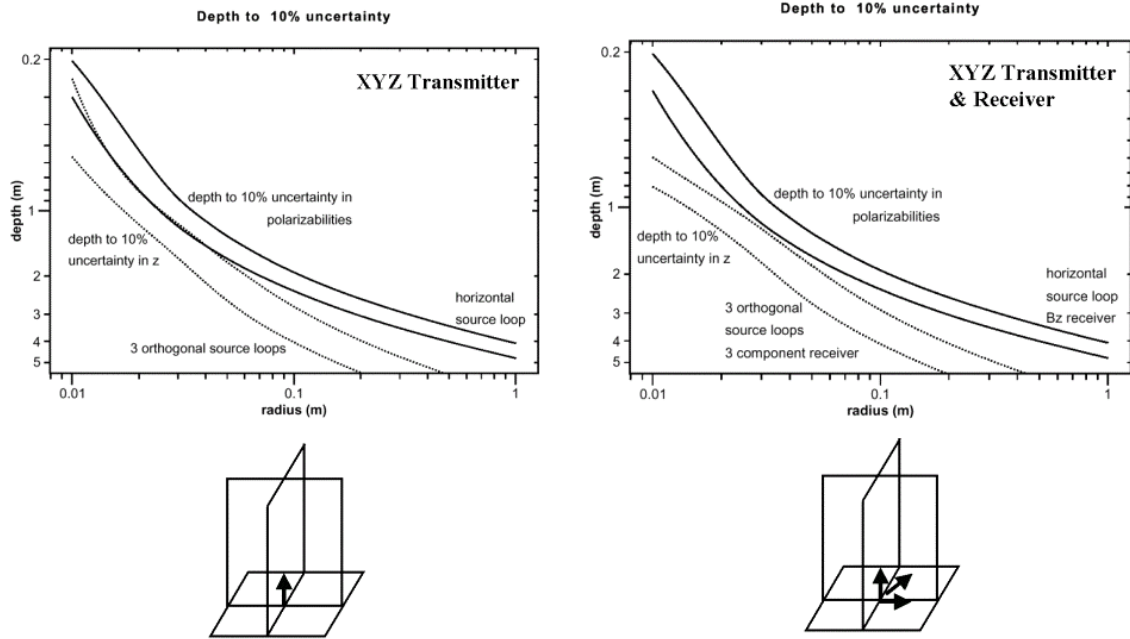
Figure 2.2.1: Depth to 10% polarizability uncertainty and 10% uncertainty in depth as a function of sphere radius for TxTyTz-Bz and TxTyTz – BxByBz systems.

The results, in Figure 2.2.1, are shown for an orthogonal three loop transmitter and vertical field, Bz, receiver and for the same transmitter with three orthogonal receivers. The results for the standard horizontal loop with a single vertical receiver are shown for reference as the solid line. The important role of multiple field polarizations at the target is easily seen in this figure. The depth of detection for a 10 cm radius sphere almost doubles with the three-component transmitter. But relatively little is gained by adding a triaxial receiver.

In general it was found that the object position can be estimated more precisely than the PDM's. The object position may be determined with only a single orientation of primary field, whereas estimating the full polarizability matrix requires illuminating the object with primary fields in at least three directions, each with a significant component in the direction orthogonal to the other two. Consequently, object depth can be resolved within 10% to greater depths than PDM's.

The recovery of the PDM's requires measurements using several polarizations of the incident field. How these are provided is a function of the spatial deployment of a system as well as the number of polarizations provided by different transmitters in the system. If a single horizontal loop source is moved in discrete intervals over an object then

it is illuminated with different polarizations by virtue of its changing position in the source dipole field. This is illustrated in the cartoon of Figure 2.2.2.
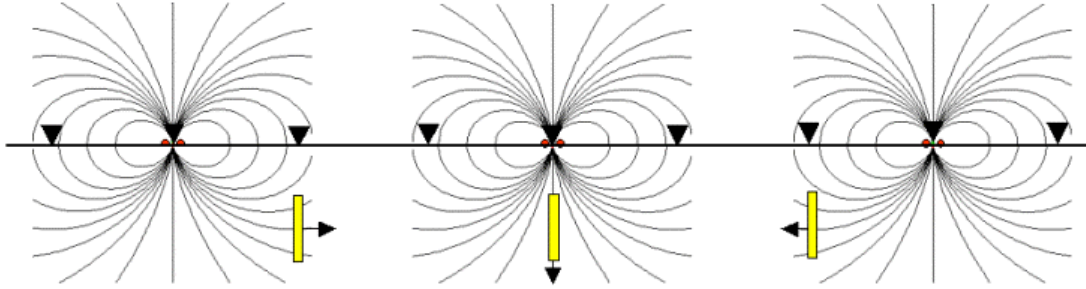
Figure 2.2.2

In the numerical experiments by Smith et al. (2002) referred to above, the 'data' were in fact assumed to have been taken on a grid. An illustration of the effectiveness of an elementary system employing a single horizontal loop receiver within a horizontal loop transmitter is shown in Figure 2.2.3.
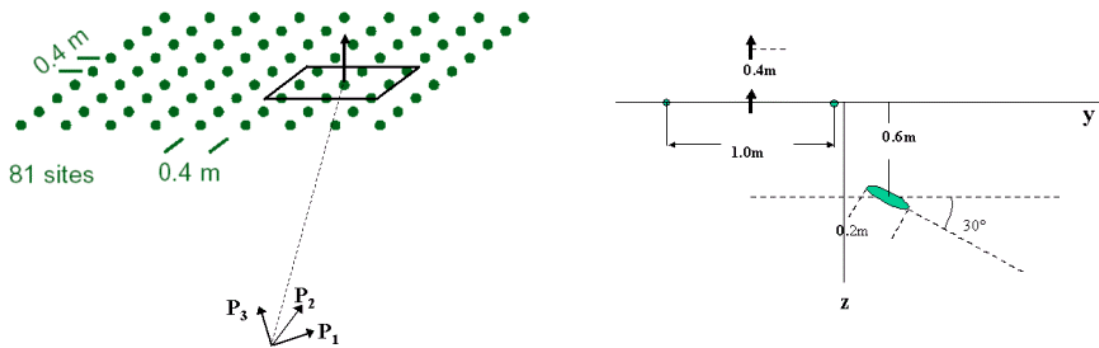
	Model			Inversion		
Location (x,y,z)	0.2	0.2	-0.6	0.207±.008	0.206±.009	-0.600±.005
PDM $(M_{x'},M_{y'},M_{z'})$				0.785±.023	0.768±.018	0.529±.011
Orientation Vector (x_1,x_2,x_3)	0	0.866	-0.5	0.016±.023	0.850±.026	-0.526±.043

Figure 2.2.3: Principal polarizations (PDM) and location for a dipping ellipsoid on 9 x 9 grid using a single horizontal loop receiver within a horizontal loop transmitter.

The target is a dipping ellipsoid and the response is obtained on a 9 by 9 grid above it. The table shows that the principal polarizations (called PDM's in this figure) and location are very well recovered. In this inversion instrumentation noise was included but location errors were not. The accuracy of the inversion now depends on accuracy of the positioning on the grid. We have addressed the role of positioning error in this project and some examples are presented below. For rapid field surveys absolute positioning to the centimeter level might be expensive and difficult but relative positioning on the scale of the target depth might be easier to achieve. This suggests designing systems which are as close as possible to stand alone: multiple transmitters and a number of spaced apart receivers that locate and characterize the target from a single system set-up in the vicinity of the target. Such a system also suggests a search procedure involving two modes of operation. First, the object is located with a simple configuration and low power, narrow band, mode. Once located, the system switches to broadband, multicomponent mode and the accurate depths and PDM's, and identification through the look-up catalog of object parameters. Finally, anticipating the results presented below, a system comprising multiple receivers will require sensors that are smaller than the loop receivers currently employed. This observation has led us to evaluate a whole new class of magnetic field detector described in the section on sensors below. In this report we analyze a variety of system configurations that are optimum for detecting objects and for determining their PDM's while minimizing their complexity and minimizing the number of sensors required.

The general simulation/inversion code was used to investigate the number of receivers, and their orientations, required for an optimum measurement of the principal polarizabilities and depths. In general, it was found that the object position can be estimated more precisely than the PDM's for the same object depth. The object position may be determined with only a single orientation of primary field, whereas estimating the full polarizability matrix requires illuminating the object with primary fields in at least three directions, each with a significant component in the direction orthogonal to the other two. Consequently, object depth can be resolved within 10% to greater depths than PDM's with the same uncertainty. The following brief description and examples are taken from a

comprehensive analysis of this problem that is discussed in more detail in a paper by Smith et al. (2003) that is being prepared for submission.

In this analysis, transmitter systems are comprised of one or several rectangular loops of fixed size, and a number of receiver coils approximated as point measurements. Three families of designs are presented: a) systems for use on a 2-D grid of positions with negligible error in relative instrument location, b) systems for use on a line of positions with negligible error in relative instrument location, and c) systems for stand alone use, insensitive to instrument positioning errors.

The general approach is summarized with reference to Figure 2.2.4 for a 2D grid of data. The color plot shows the uncertainty in the determination of the principal polarizabilities for a test object (in this case a sphere for ease of illustration) of various diameters. The data for the inversion are the responses for the simple in-loop configuration (similar to the commercial EM 61 system) at 81 positions of the 9 x 9 grid shown on the right. The contours are drawn at locations in the vertical section beneath the array where the uncertainty in polarizability is equal to the polarizability itself – in effect a signal to noise ratio of one. As mentioned above the depth can be determined with any specified uncertainty at greater depth than the polarizability. Using Figure 2.2.1 as a guide, the depth of a 60 mm sphere can be determined to within 10% at a depth 50% greater than depth at which the polarizability is determined to within 10%. Consequently the contours in plots like those of Figure 2.2.1 can be used as rough measures of the depth of detection of the relevant object. For example the polarizability of a 40 mm sphere could be determined with an uncertainty of less than its polarizability anywhere in the section above the contour labeled 40 mm but the depth would be well determined above this contour. The 40 mm sphere would consequently be well located anywhere to a depth of about one meter and in a swath of plus or minus 1.0 m around its horizontal position. In comparing configurations for a specific target, the 'best' are those for which the contours for that target's diameter are deepest in the section and flattest. We have found this graphic presentation to be an excellent way to illustrate the range and accuracy of a particular configuration of transmitter and receiver.
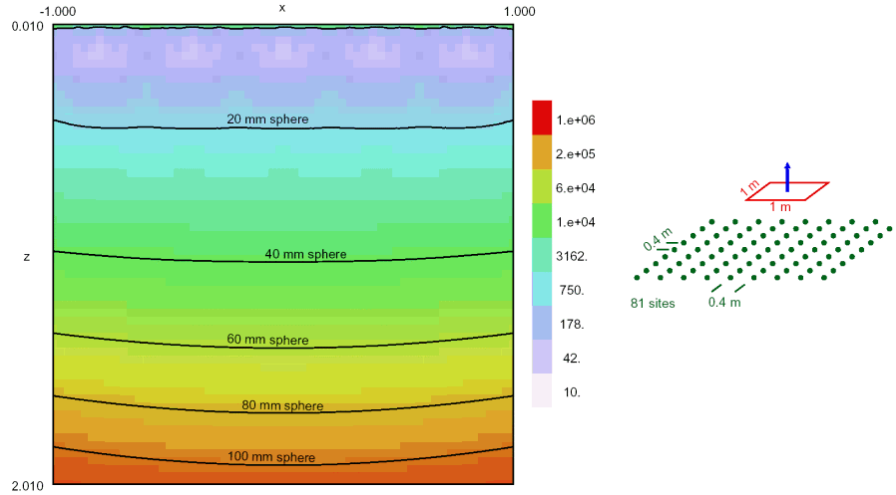
Figure 2.2.4: Rms uncertainty in polarizability as a function of position on 9 x 9 grid using simple in-loop configuration.

The improvement in detectability that accrues from using multiple transmitters and receivers is evident in the results shown in Figure 2.2.5 for a configuration with 3 orthogonal transmitters and 3 orthogonal receivers deployed on the same 9 x 9 grid. The detectability of the 40 mm sphere is pushed down to 1.5 m and the 80 mm sphere, previously detectable to 1.5m is now pushed down, off the graph, to more than 2.0 m.

Next, in Figure 2.2.6, the uncertainty in polarizability is plotted for a simple two transmitter three receiver (vertical) configuration deployed at 21 positions along a line over the target. In this and subsequent multi receiver configurations the inversion code was used to determine the location of the receivers that optimized the resulting uncertainty plot. We found that the orientation of the sensors was less important than the number used and their spacing. Since we have observed that ambient EM noise fields are predominantly in the horizontal plane, we have elected to use vertical receivers in the array studies. Further, to minimize the footprint of the system we imposed penalties on the inversion for receivers outside the perimeter of the horizontal transmitter.

The results for the line system indicate that the depth range is reduced a little and the swath width is considerably reduced over the grid system of Figure 2.2.5. Nevertheless it is important to note that comparable results would be obtained if successive lines were run with line spacing of 0.5 m. The grid after all could be considered as multiple parallel lines with spacing of only 0.4 m. If survey cost is proportional to the number of readings

then there are appreciable savings in the multi-element line profiling. We will return later to the role of position uncertainty in this assessment.
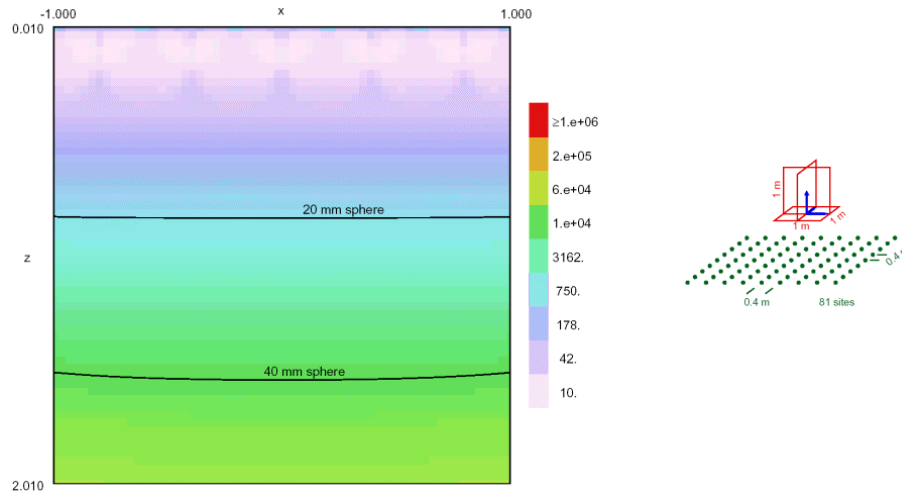
Figure 2.2.5: Rms uncertainty in polarizability as a function of position on 9 x 9 grid using 3 orthogonal transmitters and 3 orthogonal receivers.
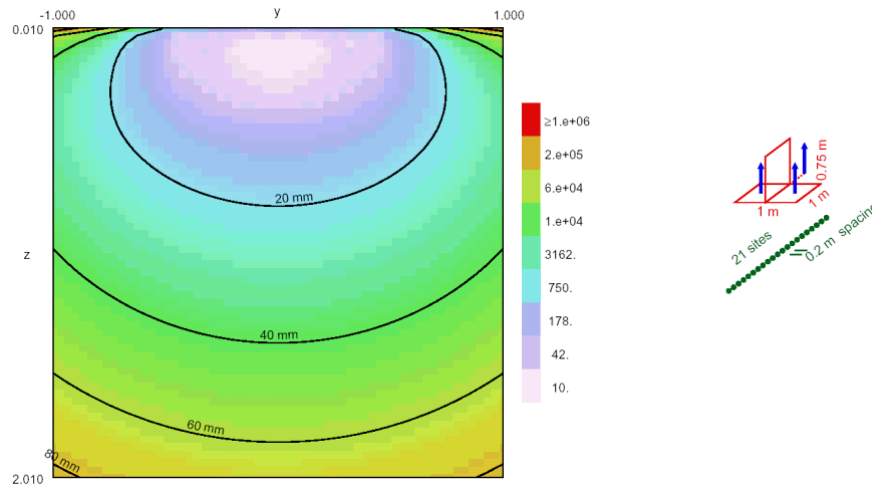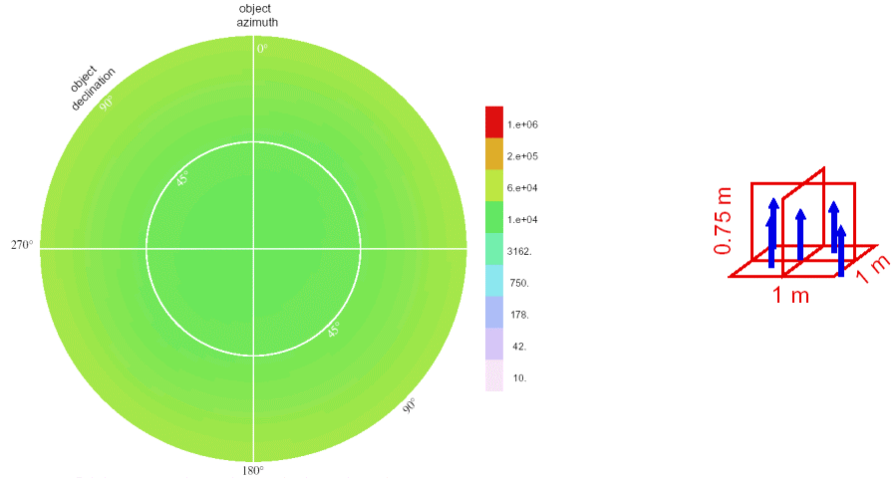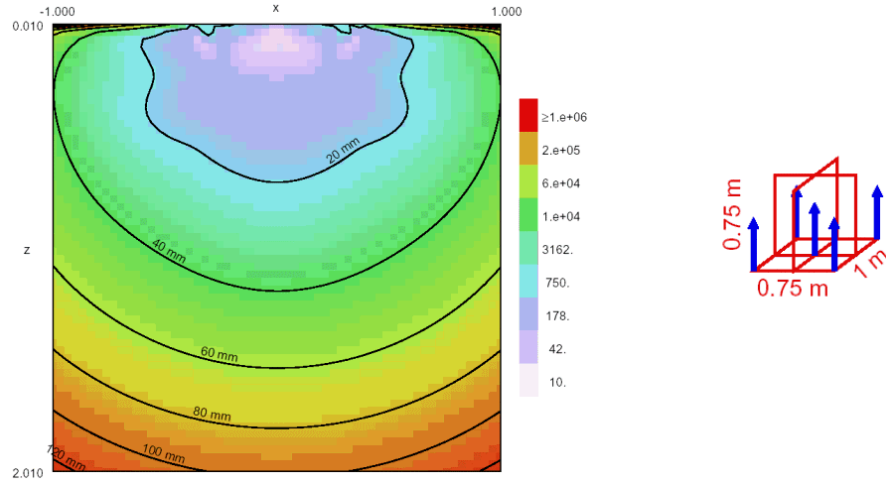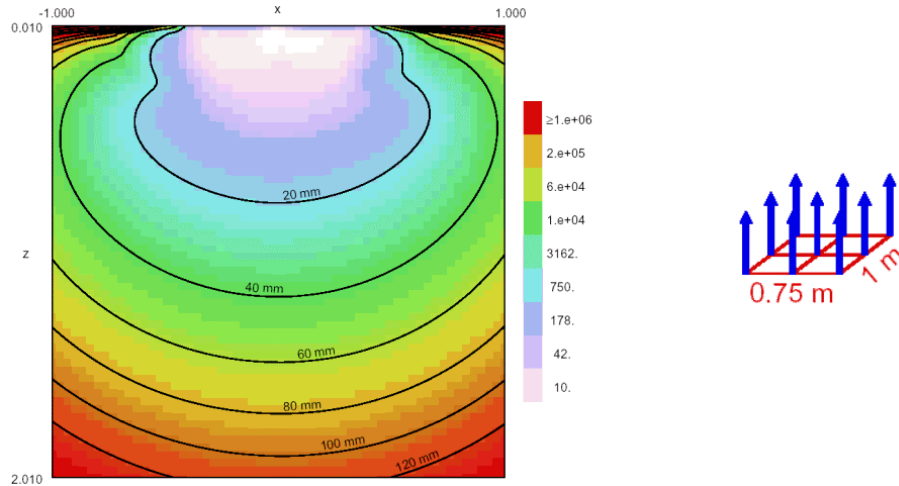

Figure 2.2.6: Rms uncertainty in polarizability as a function of position using two transmitters and three receivers in a profile mode.

Finally we experimented with single or stand alone configurations which could determine depth and polarizations from a single position in the vicinity of the target. In all these systems we used a three component transmitter. The results for a four receiver configuration are shown in Figure 2.2.7. The depth of detection is reduced somewhat and the pattern is narrowed and skewed. Another important measure of the design process is illustrated for this array in the plot of Figure 2.2.8. Here the uncertainty in polarizability is

plotted as a function of orientation of an elongate target at a depth of one meter. The plot clearly shows that there are 'blind spots' for this configuration – orientations for which the number of T-R pairs is inadequate to determine the orientation. Smith et al. (2003) have determined theoretically that 13 T-R pairs are required to determine the polarizabilities so the 12 pairs are in fact not enough. Adding a fifth receiver, in the optimized five element array of Figure 2.2.9, makes a dramatic improvement in the orientation determination. Even at a depth of 1.6 m there are no blind spots for this array as seen in Figure 2.2.10, although there is only a modest improvement in the depth of detectability, Figure 2.2.9.
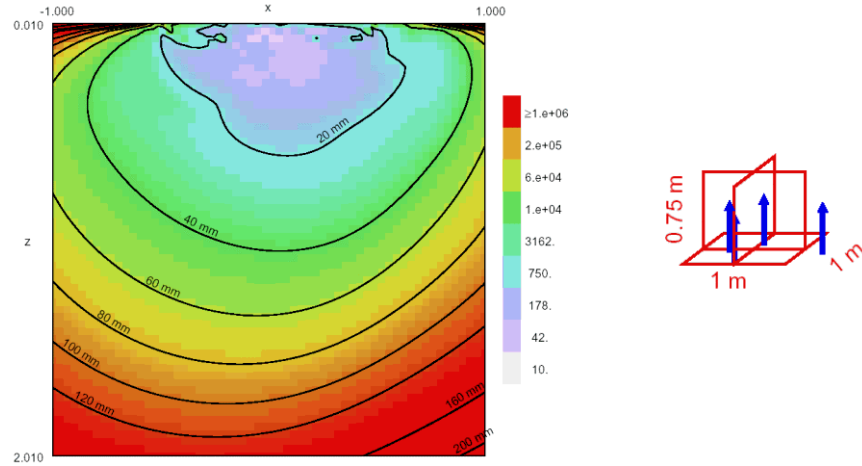
Figure 2.2.7: Rms uncertainty in polarizability as a function of position using three transmitters and four receivers in a stand alone mode.
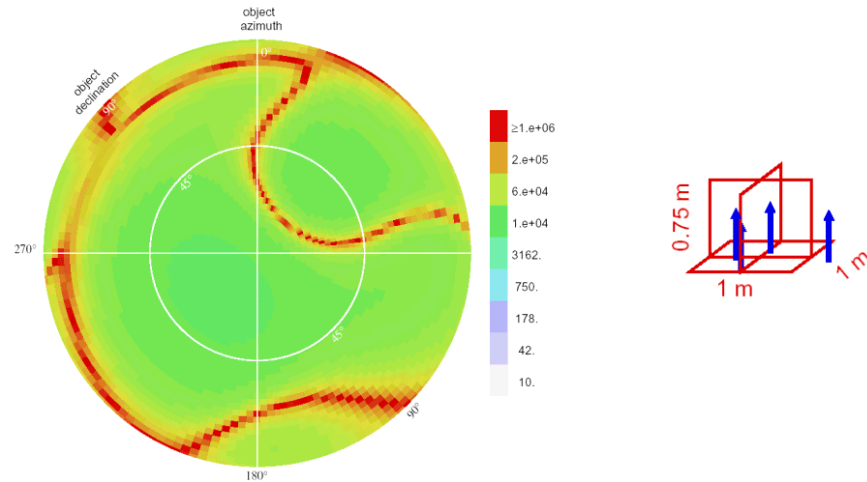
Figure 2.2.8: Rms uncertainty in polarizability as a function of orientation of an elongate target at a depth of 1 m.

18
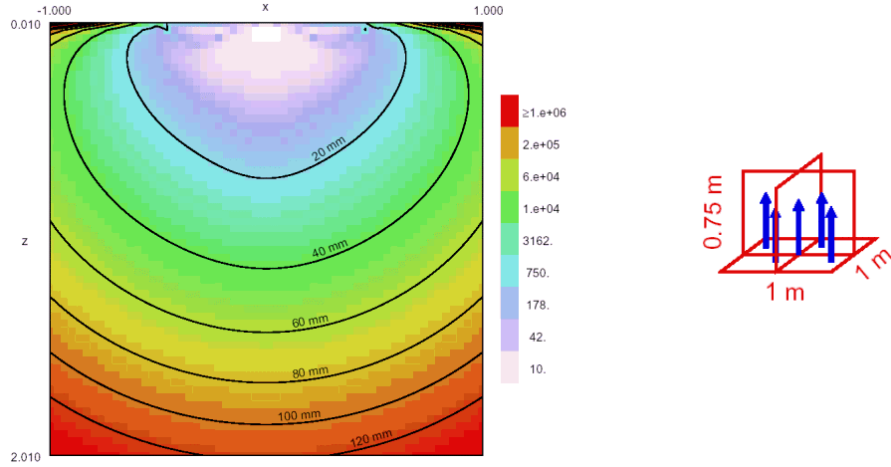
Figure 2.2.9: Rms uncertainty in polarizability as a function of position using three transmitters and five receivers in a stand alone mode.

Figure 2.2.10: Rms uncertainty in polarizability as a function of orientation of a target at 1.6 m depth using three transmitters and five receivers in a stand alone mode.

Allowing the inversion code to 'choose' the location of the vertical receivers results in a rather irregular pattern as shown on the right of Figure 2.2.9 as an example. From a fabrication viewpoint it might be simpler to arrange the sensors in a regular pattern dictated by the frame or structure of the transmitters. We tried the regular pattern of Figure 2.2.11 and found very little reduction in detectability compared to the optimum pattern. The conclusion of studies such as this is that optimization is not a strong function of variation of sensor position around the optimum one.

Figure 2.2.11: Rms uncertainty in polarizability as a function of position using three transmitters and five receivers in a regular pattern dictated by transmitter frame.

Some prototype AEM systems have employed an ingenious combination of horizontal loops to provide both a vertical and horizontal polarization of the incident field at a target beneath the array. In Figure 2.2.12 the horizontal loops consist of four independent rectangular loops and a redundancy of 9 vertical receivers. When two adjacent loops are energized with the same, say clockwise, current flow they sum to produce an equivalent large loop of the same polarity which produces a primary field directed vertically beneath the center of the loop. When energized with opposing current flows a multipole field is produced with field lines that are horizontal beneath the loops. Similar energization of the orthogonal pair of loops produces the requisite third, horizontal, polarization of the field incident on the target.

The results (Figure 2.2.12), even with 9 receivers, are not as good as those obtained with the transmitter consisting of three orthogonal loops and 5 receivers, Figure 2.2.11.

Finally, to close the loop on these illustrative examples, it is important to note that the depth of detectability for the 3 transmitter 5 receiver stand alone system, Figure 2.2.11, is almost as good as the 3 transmitter 3 receiver system when the latter is deployed at 21 positions along a line or profile. It is also almost as good as the current industry standard EM61 system when the latter is deployed on a grid of 81 points, Figure 2.2.4. On the other hand it is not nearly as good as the 3 transmitter 3 receiver configuration deployed on the same grid, Figure 2.2.5.

Figure 2.2.12: Rms uncertainty in polarizability as a function of position using four independent horizontal loops and 9 vertical receivers.

The results to date were obtained assuming that there were no errors in the position of the system on the grid or along the line. In a practical survey there are such errors, largest in the absolute position on the grid, less in relative position along a line segment and zero for the stand alone system (the latter finds the polarizability and the target location relative to the T-R system so the uncertainties are proportional only to the system noise). Figures 2.2.13 and 2.2.14 display the relative uncertainties in polarizability and depth respectively as a function of the position error for the three deployment arrays shown on the right of the figures. The statistics were created by repeated inversions with random misplacements of each measurement point by the indicated position error. The target in this experiment was a horizontal 22 mm shell with an aspect ratio of 8:1 at a depth of 0.75 m. The relative uncertainties in polarizability and depth for both the line and grid configurations remain less than that of the stand alone system (about 5%) as long as the position uncertainty is less than about 2 cm. Relative GPS positioning is at best a few cm so without expensive and logistically difficult laser or microwave positioning it appears that the stand alone system is superior to line and grid deployments. But the stand alone system can also be operated in line or grid mode the results of which would be significantly better than any of the individual schemes discussed till now. Since the stand alone system has the same footprint as the best current commercial system, the field operational issues are identical to the current systems but with vastly improved detection and identification

properties. Further the system retains excellent detection and polarization determination from irregularly located single positions, which may be all that is available in terrain with obstacles to regular grids or profiles.
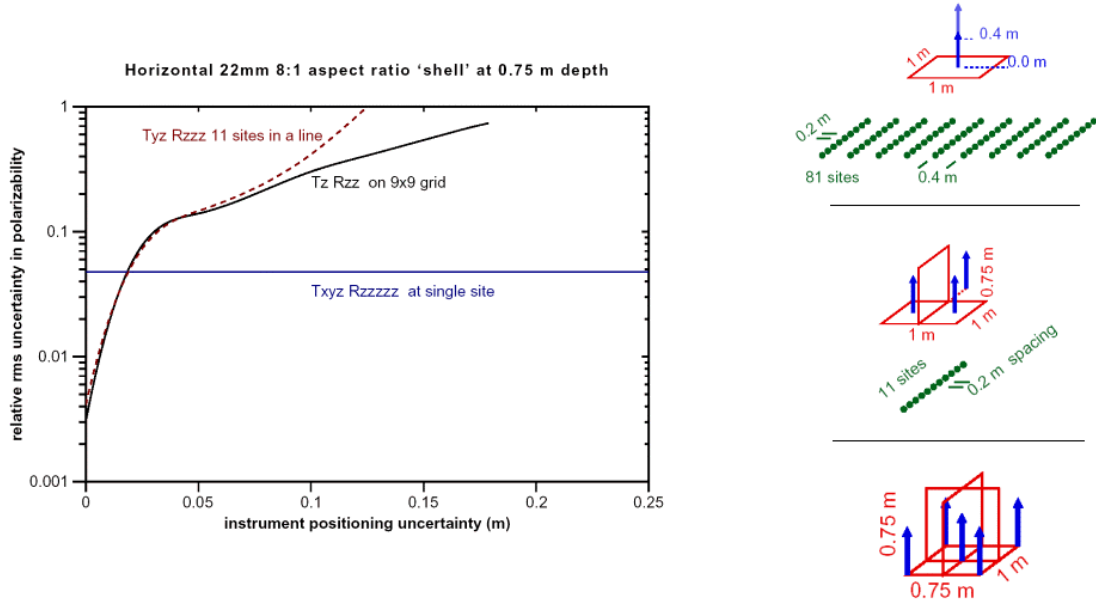
Figure 2.2.13: Relative rms polarizability uncertainty as a function of instrument location error for 22 mm 8:1 aspect ratio shell at 0.75 m depth at 610 μs after transmitter shut-off.
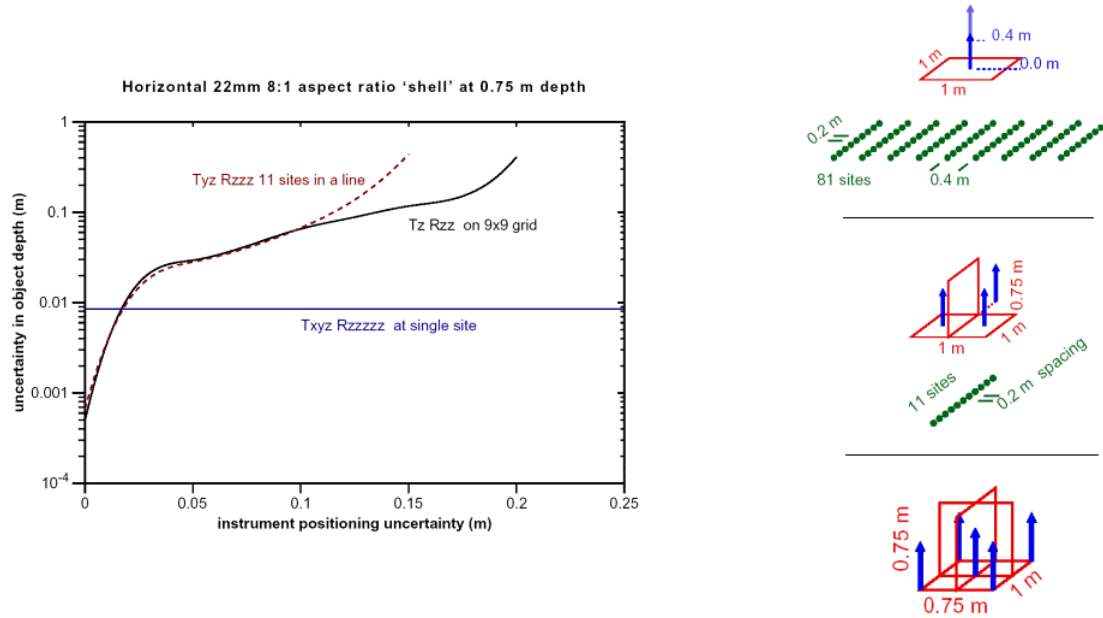
Figure 2.2.14: Relative rms depth uncertainty as a function of instrument location error for 22 mm 8:1 aspect ratio shell at 0.75 m depth at 610 μs after transmitter shut-off.

2.3 Spectral properties of target response

The analysis till now has concentrated on the detection of a target, and the determination of depth and principal polarizabilities of the target. In the introduction we also described the vital step of measuring the polarizabilities as a function of frequency, or time, to determine the shape, size, metal content and even the wall thickness of the object. Only the variation of the induced moments with frequency permit the determination of the various shapes shown in the cartoon of Figure 2.1.1. This analysis immediately raises the issue of the necessary bandwidth. To get an idea of the bandwidth over which the principal polarizabilities undergo their defining variation we again turned to the simulator to find the spectral and transient responses for some typical UXO.

The response of a target is defined here as the secondary field (B) at a given receiver for an incident field from a given transmitter. The response is thus a function of the T-R pair as well as the properties of the target. Induction coil sensors typically measure the time derivative of the secondary field B so the dB/dt response is often used.
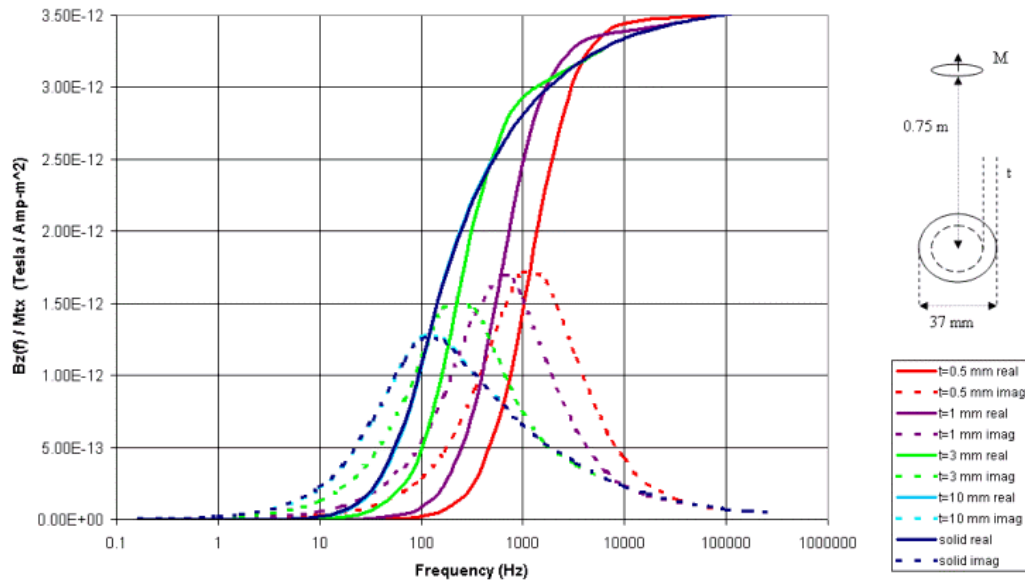
Figure 2.3.1: Normalized secondary fields (real and imaginary components) as a function of frequency for 37 mm aluminum spherical shell of various thicknesses at 0.75 m depth.

To illustrate the spectral response of a variety of targets, we have chosen to use a simple horizontal loop transmitter with an in-loop vertical receiver deployed directly above the target. This is basically the model for the EM61 commercial system. This configuration, the target size and shape, and the separation of the T-R system from the target are shown to the right of the response plots in the following figures. In all cases the secondary fields in nano-Tesla (nT) are normalized by the transmitter moment. We have plotted the frequency response real (or in-phase) and imaginary (out of phase or quadrature) and the transient response for B and dB/dt to illustrate diagnostic behaviors in both domains. We have studied the response of non-magnetic conductors as well as the more common permeable conductors and for the simple sphere we have analyzed the effect of changing shell thickness on the response.

The first analysis shows the effect of shell thickness on the frequency response of an aluminum 37 mm spherical shell 0.75 m below the T-R pair. For any body the high frequency response, so called inductive limit response, depends only on the size. In the frequency domain, variations in the shell thickness produce characteristic changes in real and quadrature response at frequencies in the decade above and below the frequency of peak quadrature response. In Figure 2.3.1 this band is between 30 and 3000 Hz. The high frequency could be estimated at a frequency of 10 kHz so an ideal bandwidth for identifying this target would be 30 Hz to 10 kHz or 2.5 decades.

In the time domain, Figure 2.3.2, the step function response in B clearly resolves thicknesses from the early time asymptote at 3×10^{-5} sec (which also determines the size) to about 3×10^{-3} sec. The thinnest shell has a pure exponential decay while the solid sphere has a 'stretched' response becoming exponential only beyond 10^{-3} sec. The sensor need only have a dynamic range of 1.5 decades to resolve the response.

The time derivative dB/dt, measured by standard induction coil sensors, is shown in Figure 2.3.3. Diagnostic changes in the response occur between 3×10^{-6} and 10^{-2} Hz — a much wider bandwidth than that for B and a dynamic range of at lest 2.5 decades is required to define the responses.
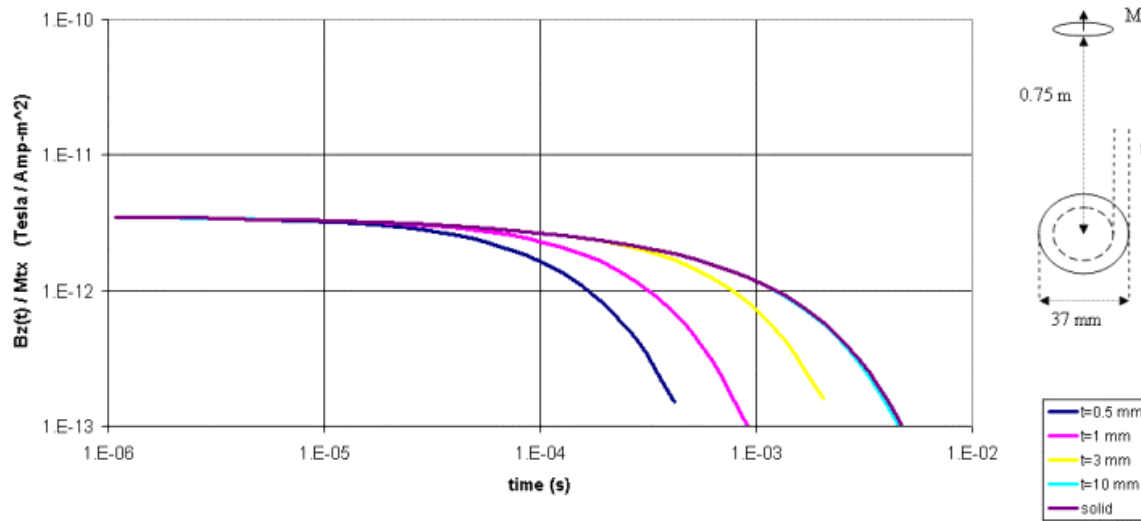
Figure 2.3.2: Normalized magnetic field response as a function of time for 37 mm aluminum spherical shell of various thicknesses at 0.75 m depth.
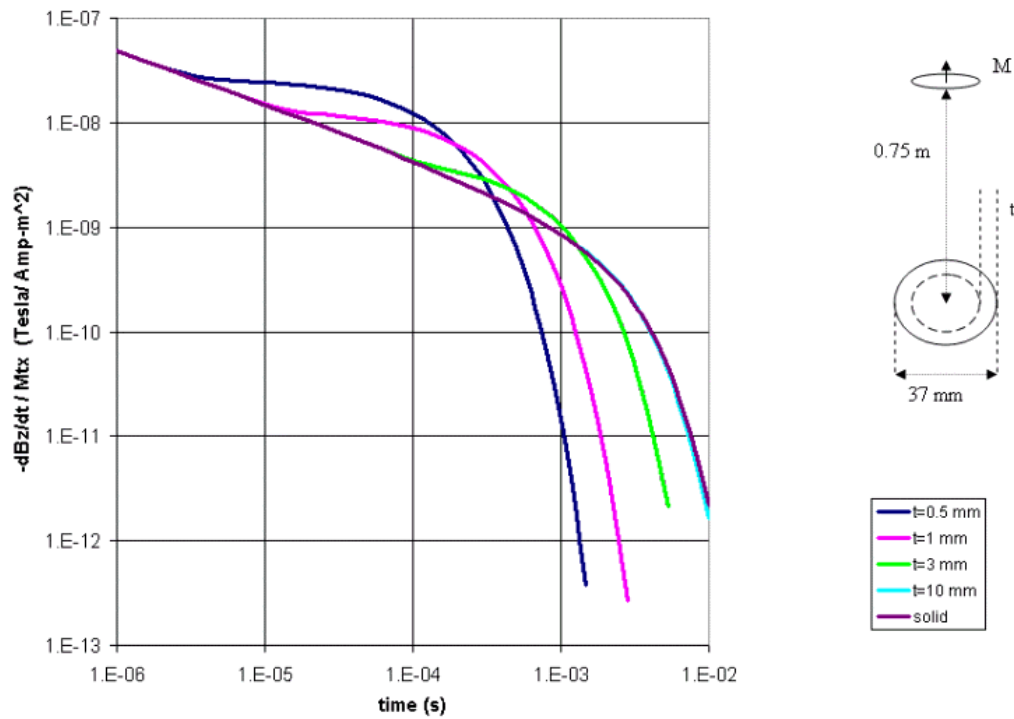

Figure 2.3.3: Normalized dB/dt response as a function of time for 37 mm aluminum spherical shell of various thicknesses at 0.75 m depth.

The frequency domain response for the same spherical shells but with a magnetic permeability of 200 is shown in Figure 2.3.4. The permeability introduces the opposing static magnetization which drives the real response negative at low frequencies and causes small perturbations in the quadrature response also at low frequencies. Resolution of shell thickness for a magnetic target is only possible at frequencies below about 300 Hz. This simple model provides the first evidence that it may be difficult if not impossible to resolve shell thickness in magnetic targets in the frequency domain.

The prospect is improved considerably in the time domain for B as shown in Figure 2.3.5. As expected, the thickness variations are manifested at late time, between 10^{-5} sec and 10^{-3} sec. The thinnest shell develops an exponential decay by 3×10^{-5} sec while the solid hasn't become exponential by 10^{-3} sec. The intervening thicknesses could be well resolved with a dynamic range of 2 decades. The resolution of shell thickness with dB/dt is markedly less than with B, Figure 2.3.6. Curve separation is clear over only one decade of time, 10^{-3} to 10^{-2} sec, and over 3 decades of amplitude but the diagnostic separation only begins after over two decades of amplitude decay from shut-off.
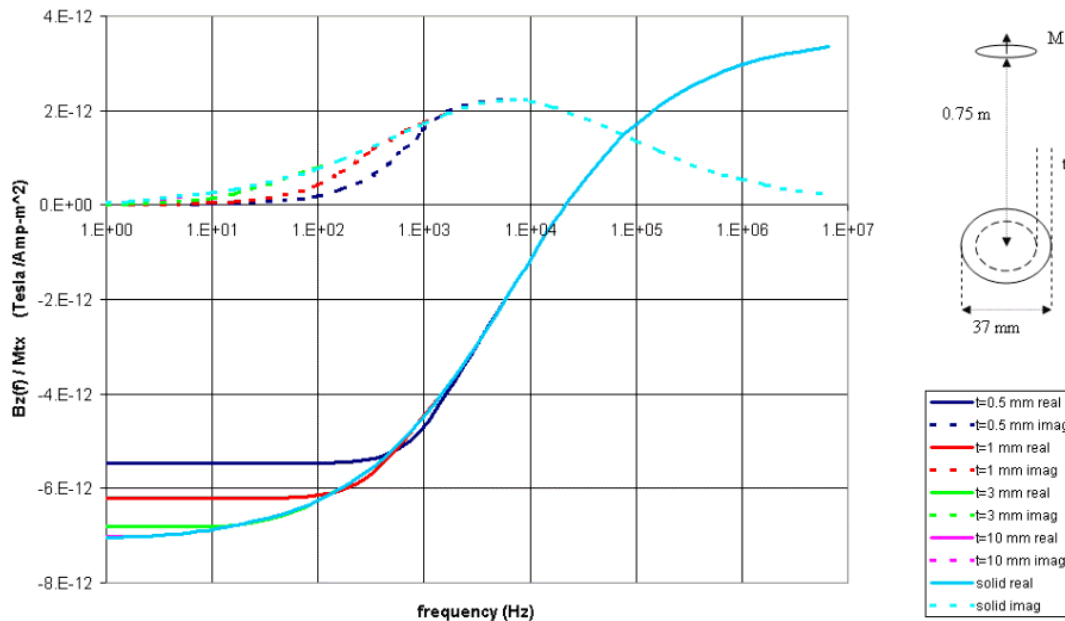
Figure 2.3.4: Normalized magnetic field response as a function of frequency for 37 mm magnetic spherical shell of various thicknesses at 0.75 m depth.
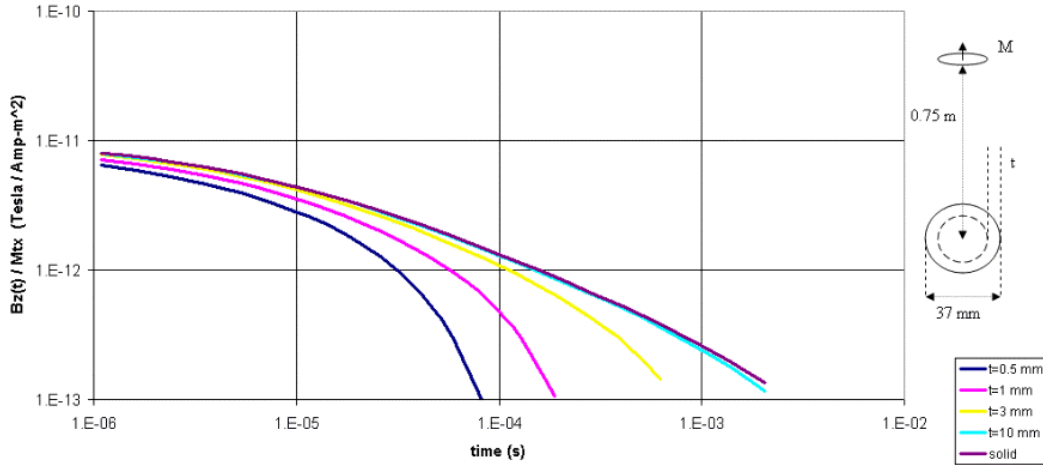
Figure 2.3.5: Normalized magnetic field response as a function of time for 37 mm magnetic spherical shell of various thicknesses at 0.75 m depth.
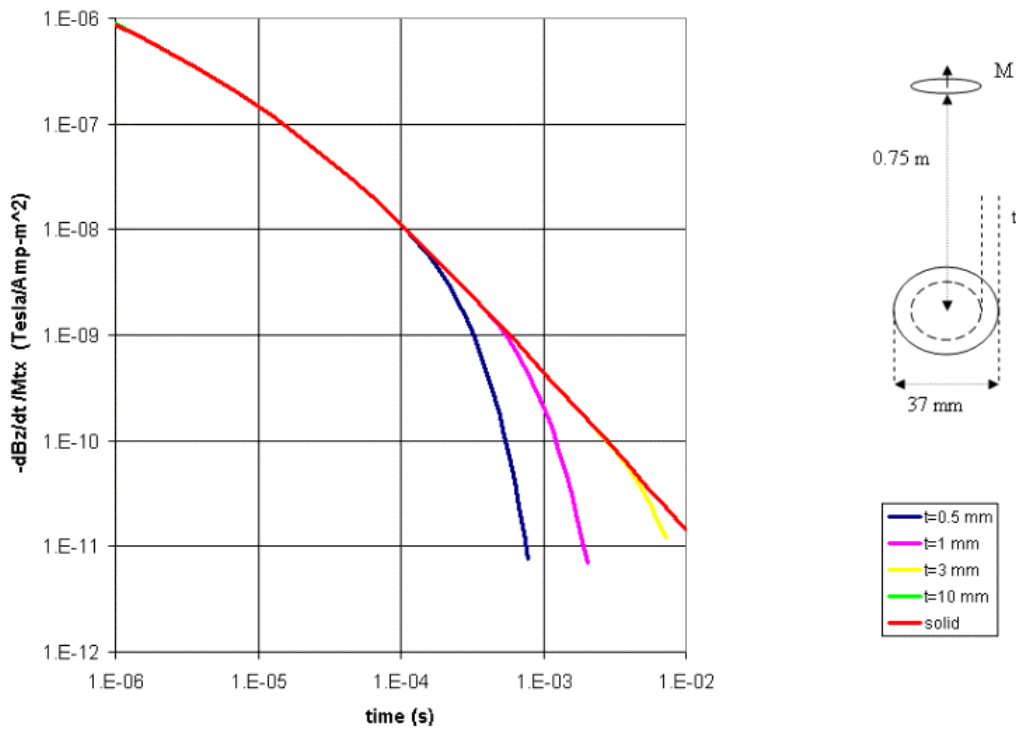
Figure 2.3.6: Normalized dB/dt response as a function of time for 37 mm magnetic spherical shell of various thicknesses at 0.75 m depth.

These sample models illustrate some general practical conclusion: B rather than dB/dt is more diagnostic of shell thickness for magnetic and non-magnetic objects, and shell thickness would be difficult to resolve in the frequency domain.

The general analysis for optimizing the T-R configuration in Section 2.2 used idealized dipoles (spheres) as the target. It is important to know how well these results apply to the case of actual, usually elongate, UXO. In Figure 2.3.7 we have shown the simulated results for an EM61 style in-loop system over a typical 37 mm shell 0.75 m below the system. The shell is solid, steel, and has an aspect ratio (length/diameter) of 3:1. The plot shows the dB/dt response for both the horizontal and vertical orientation of the shell. For comparison the response of the 37 mm sphere is included. It is immediately evident that the actual shell response, for both orientations, is larger than the sphere responses. It may be concluded that all the detectability analyses of Section 2.2 are worse case scenarios and so are excellent design guides for a working system.

In Figure 2.3.7, and subsequent plots for other targets, we have also plotted the response from the conductive ground in which the target is immersed. The responses for two ground resistivities, 10 and 100 Ohm-m, are plotted. The ground response basically imposes an early time limit on the time window available for target discrimination. Once the target response falls below the ground response it will be poorly resolved, especially since the ground response itself will variable due to the inhomogeneous nature of the near surface. (The role of magnetic ground is still being analyzed and will be described in a later report.) For a conservative design approach we assume a ground of 10 Ohm-m.
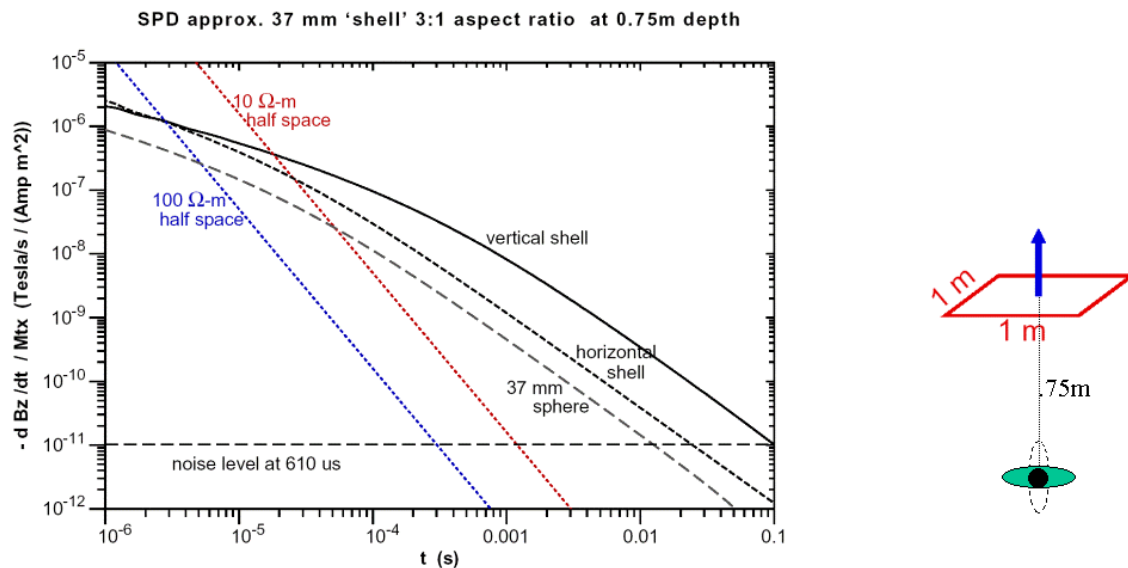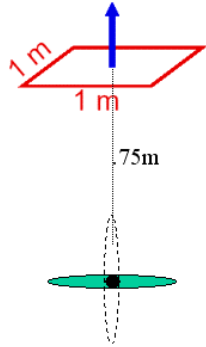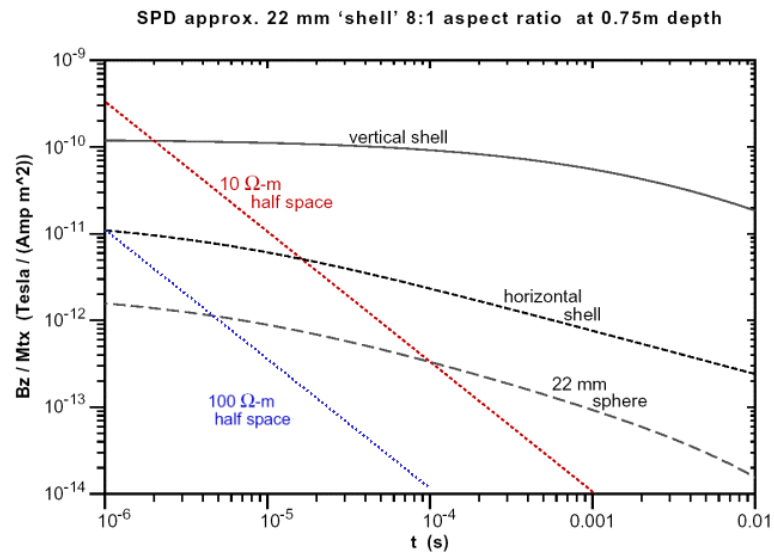

Figure 2.3.7: Amplitude of dB/dt response for 37 mm sphere, horizontal and vertical shells 3:1 aspect ratio at the depth of 0.75 m as a function of time together with responses for 10 Ω-m and 100 Ω-m half-space.

For this EM61 simulation we can also include the normalized practical noise level for this system at 610 μsec. Since the noise level is not known at other times into the transient, we have simply assumed that the noise is constant at this level for all times and plotted this horizontal noise floor accordingly.

The early time limit imposed by the ground and the later time limit imposed by the noise sets the time window over which the response can be measured. For this target the window is roughly from $2x10^{-5}$ to $3x10^{-2}$ (for the horizontal shell). Referring back to Figure 2.3.6, it can be seen that this window is adequate to define the size (early time asymptote) of the sphere and to resolve its thickness, but the dynamic range is almost five decades above the noise floor. This may be difficult to achieve in practice. Using only the later time data, say from $2x10^{-4}$ sec, may be satisfactory especially since it should be noted that the orientation has already been determined in the first stage of the inversion.

The response of this elongate target also reveals the fact that the frequency response is different for the different polarizabilities of a non-spherical target. The responses of the horizontal and vertical orientations of this 37 mm shell actually cross at a few microseconds, the horizontal shell giving a longer response at very early time than the vertical shell. This is an excellent illustration of the fact that the ratio of the polarizabilities is not the same as the geometric aspect ratio of the body. As can be seen in Figure 2.3.7 the ratio of the horizontal and vertical responses at later time is 10:1. (An interesting observation is that the ratio of the horizontal responses for the target to that of a sphere of the same diameter is 3:1. This appears to hold true for all the elongated targets we considered. The result holds for the B response as well.)

For B rather than dB/dt the window where the target response exceeds the ground response widens to $3x10^{-6}$ sec at the low end, Figure 2.3.8. Since there are no existing systems that measure B we have no estimate of when the late time response meets the noise floor. However, the horizontal and vertical responses still differ by a factor 10 and most importantly the observed separation (including very early time) is confined to less than 3 decades of amplitude variation. Instrumentally this is much more manageable than the much higher dynamic range required for a dB/dt system.

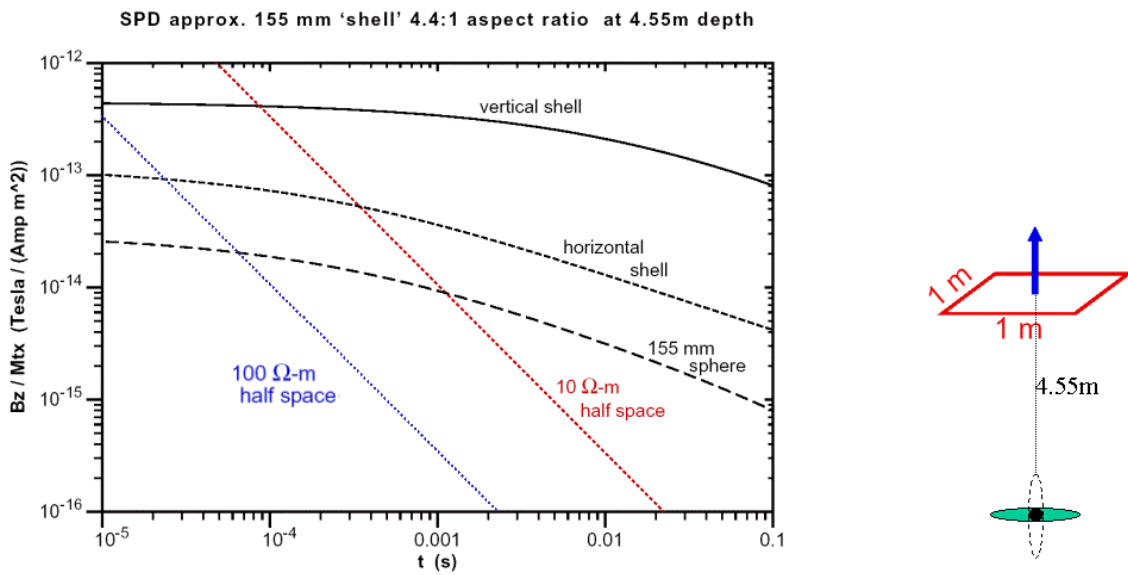**SPD approx. 37 mm 'shell' 3:1 aspect ratio at 0.75m depth**
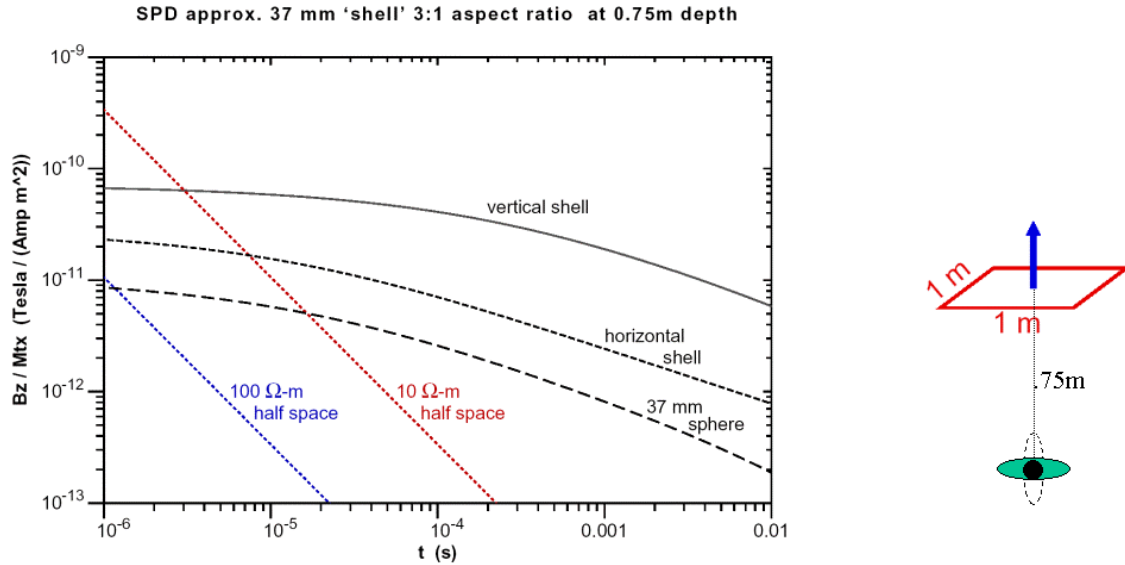
Figure 2.3.8: Amplitude of magnetic field response for 37 mm sphere, horizontal and vertical shells 3:1 aspect ratio at the depth of 0.75 m as a function of time together with responses for 10 Ω-m and 100 Ω-m half-space.

Figures 2.3.9 through 2.3.14 show the B and dB/dt responses for three other targets representative of the extremes of UXO to be characterized – a 22 mm shell with an aspect ratio of 8:1 (Figures 2.3.9 and 2.3.10) at a depth of 0.75 m, a 105 mm shell with an aspect ratio of 4:1 at a depth of 2.65 m (Figures 2.3.11 and 2.3.12), and a larger 155 m shell with an aspect ratio of 4.4:1 at a depth of 4.55 m (Figure 2.3.13 and 2.3.14). In all these simulations the ground response limits the early time response to microseconds in B and 10's of microseconds in dB/dt. The dynamic range requirement is reduced in B and responses to at least 0.01 sec (10 msec) are required to clearly resolve the decay characteristics. For the large target at greater depth the response must be obtained to at least 100 msec at which point, at least for this sample EM61–like system, the response in dB/dt is below the noise level (see Figure 2.3.13).
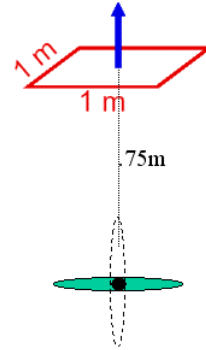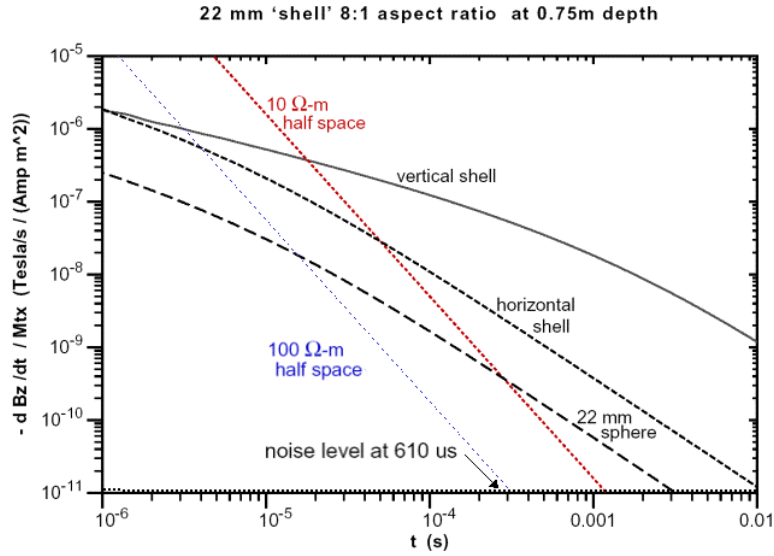
Figure 2.3.9: Amplitude of dB/dt response for 22 mm sphere, horizontal and vertical shells 8:1 aspect ratio at the depth of 0.75 m as a function of time together with responses for 10 Ω-m and 100 Ω-m half-space.

Figure 2.3.10: Amplitude of magnetic field response for 22 mm sphere, horizontal and vertical shells 8:1 aspect ratio at the depth of 0.75 m as a function of time together with responses for 10 Ω-m and 100 Ω-m half-space.
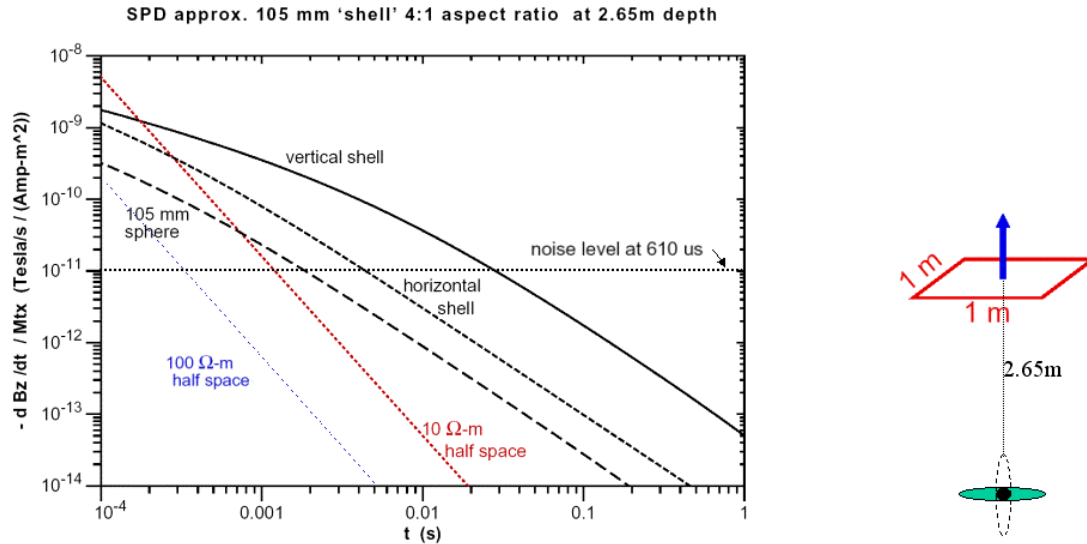
Figure 2.3.11: Amplitude of dB/dt response for 105 mm sphere, horizontal and vertical shells 4:1 aspect ratio at the depth of 2.65 m as a function of time together with responses for 10 Ω-m and 100 Ω-m half-space.
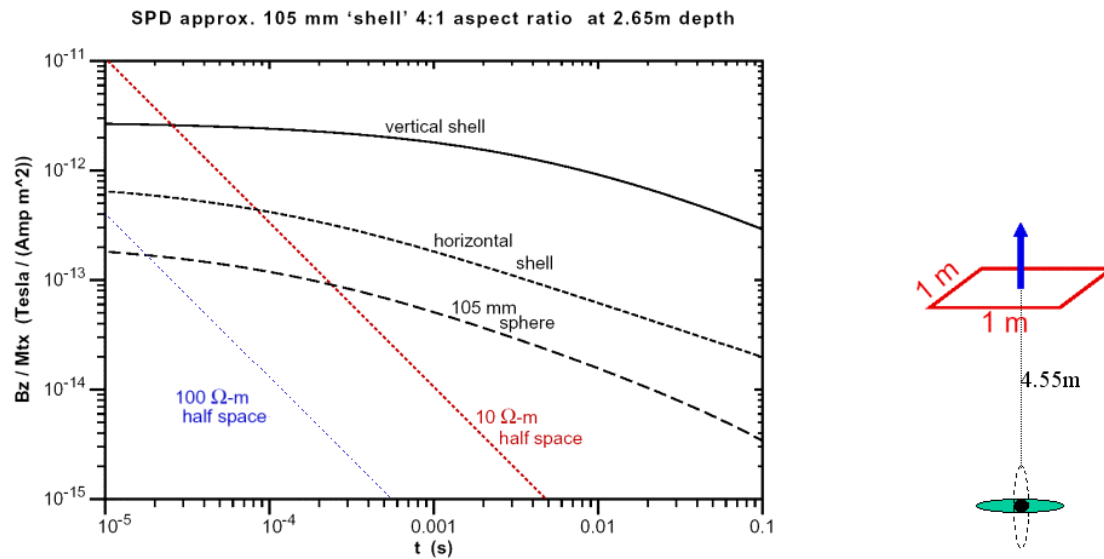
Figure 2.3.12: Amplitude of magnetic field response for 105 mm sphere, horizontal and vertical shells 4:1 aspect ratio at the depth of 2.65 m as a function of time together with responses for 10 Ω-m and 100 Ω-m half-space.

SPD approx. 155 mm 'shell' 4.4:1 aspect ratio at 4.55m depth
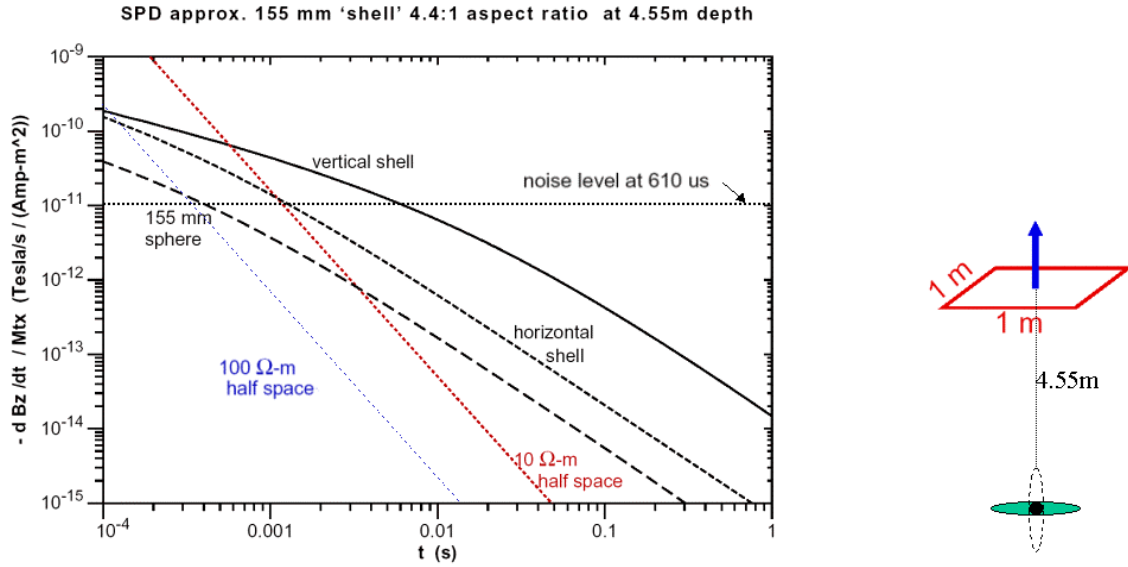
Figure 2.3.13: Amplitude of magnetic field response for 155 mm sphere, horizontal and vertical shells 4.4:1 aspect ratio at the depth of 4.55 m as a function of time together with responses for 10 Ω-m and 100 Ω-m half-space.

SPD approx. 155 mm 'shell' 4.4:1 aspect ratio at 4.55m depth

Figure 2.3.14: Amplitude of magnetic field response for 155 mm sphere, horizontal and vertical shells 4.4:1 aspect ratio at the depth of 4.55 m as a function of time together with responses for 10 Ω-m and 100 Ω-m half-space.

33

These examples have been chosen to illustrate the properties of a particular system, in this case an EM61 simulation, in resolving elongate objects at a variety of depths and in showing the time window constraints imposed by the ground response and the system noise levels. The results of Section 2.2, for example Figure 2.2.3 shows the dramatic improvement in detectability that occurs when a multi-element T-R configuration is used on a grid of stations. Figure 2.2.3 for example shows that the 155 mm target at a depth of 4.55 m would not be detectable with the simple in-loop system. This of course is also seen in Figure 2.3.13 where only the vertical 155 mm elongated shell rises above the noise in the 6×10^{-4} sec to 7×10^{-3} sec time window. Figure 2.2.3 indicates that the three transmitter - three receiver configuration, occupying many locations, could easily determine the depth and polarizabilities to better than 10% for this 155 mm target. A combination of detectability graphs such as Figure 2.2.5 or 2.2.11 and specific response plots such as those shown in the suite of Figures from 2.3.4 to 2.3.14 establish the bandwidth and moment requirements for an actual field system.

In summary, it appears that for step function excitation, transients from 10 microseconds to 100 milliseconds are to be detected for a practical range of UXO and a practical range of depths. Overall B receivers may be more effective than dB/dt receivers.

The design effort now shifts to the feasibility of making magnetic field sensors and instrumentation that can achieve measurement bandwidths (or time windows) that meet the specifications of these simulations. Further, it was shown in Section 2 that optimum determination of depth and orientation required multiple point sensors (arrays of compact sensors) and so a major design issue is to determine the feasibility of making small induction sensors to replace the large open loop sensors currently used in all AEM systems. The following sections describe our efforts to date to develop small sensors and to design the electronics for achieving the desired bandwidths.

3. SENSORS

An optimum array of receivers requires at least 5 magnetic field sensors. The simulations of Section 2 showed that 5 vertical sensors on the corners f the 1 m x 1 m horizontal square loop transmitter and another in the center would be a satisfactory deployment of the sensors. We have acquired the magnetic sensor shown in Figure 3.1. The sensor is roughly 6 in (17 cm) long, and about 1 inch (2.8 cm) in diameter. It has a high permeability ferrite core about 1.0 cm in diameter and is wound with 7000 turns of wire. It also has a concentric 200 turns winding of a feedback coil, so the sensor becomes a null detector and the feedback current in then a measure of the magnetic field. Depending on the sensor electronics the coil can be operated as a magnetic field B or dB/dt device. The sensor is manufactured by EMI, Inc., identified as a BF-6s, and is a scaled down version of their BF-6 sensor that is widely used in commercial EM systems used in mineral, petroleum, and groundwater applications.

Figure 3.1: A wide-band induction receiver with feedback (Manufacturer: EMI, Inc.).

In feedback mode the amplitude response of the sensor itself is flat (Figure 3.2), i.e. it operates as an ideal B detector, from about 400 Hz to 2×10^4 Hz. The phase changes from 45° to –45° over the same interval. Below 400 Hz the device operates as a conventional induction coil sensor. The 'flat' bandwidth is determined by the feedback electronics and can be made to go from 40 Hz to 2×10^5 Hz. The response appears to be quite satisfactory based on the requirements outlined in the simulated responses presented in Figure 2.3.1 from Section 2.3 above.
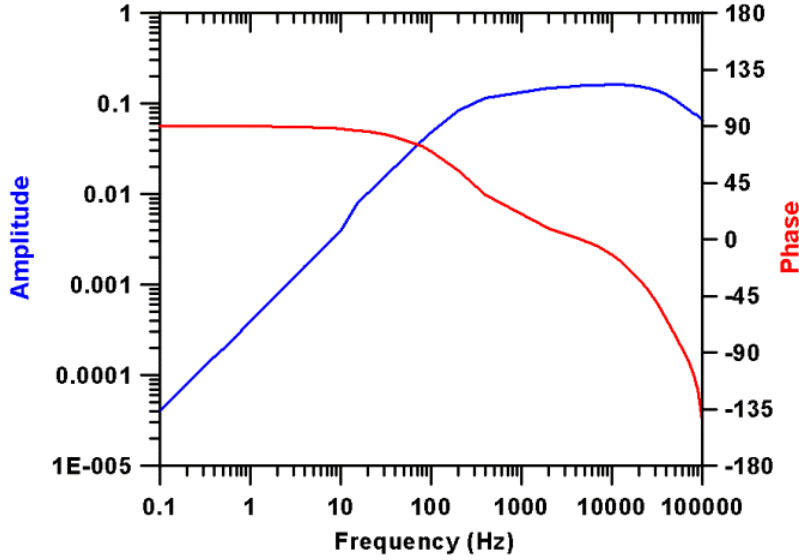
Figure 3.2: A frequency response of the wide-band induction receiver from Figure 3.1.

The noise figures for these small sensors appear satisfactory as well. The noise spectra of the short coil, BF-6s, and its longer cousin BF-6 (60 cm long), as shown in Figure 3.3 along with the noise spectrum of the acquisition system when the coil replaced with a simple resistor. This is the measured noise spectrum obtained in the field from cross-spectral measurements on two identical coils operated in parallel a meter apart. The noise of the short coil is almost an order of magnitude greater that that of the BF-6 at 40 Hz but is only half an order of larger at 10^4 Hz. The noise at 40 Hz is about 1.0 pico-Tesla (pT) / $\sqrt{Hz}$ and at 400 Hz, the lower bound of the flat response, is only $7x10^{-5}$ nT /$\sqrt{Hz}$ (or 70 femto-Tesla (fT) / $\sqrt{Hz}$). Revisiting the plot of Figure 2.3.1, showing the frequency response for the simple in-loop configuration, we find that the quadrature secondary field at 400 Hz varies from 10^{-13} to $1.5x10^{-12}$ or from 100 to 1500 fT for a transmitter moment of 1.0. In short the new sensors have a more than adequate signal to noise ratio in the bandwidth required to detect and characterize the typical UXO that we have considered.
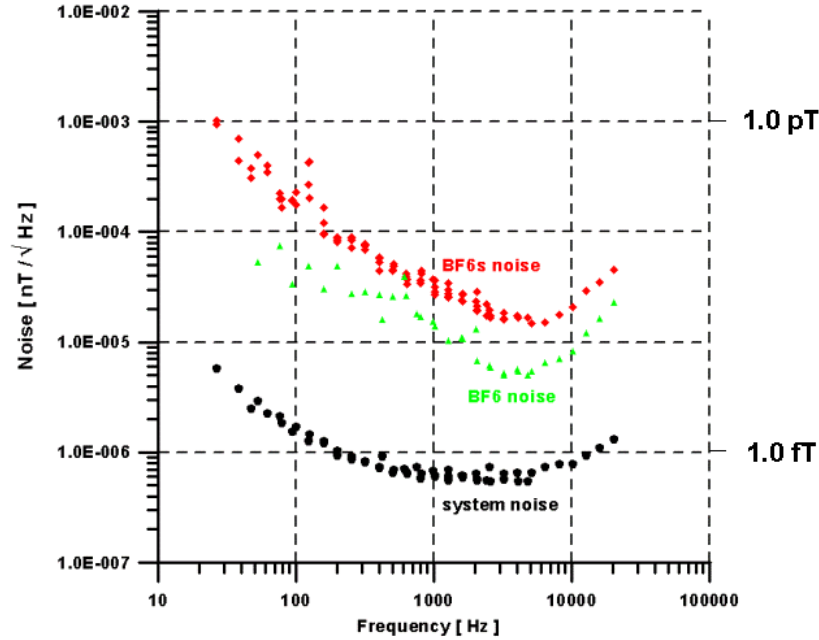
Figure 3.3: Noise levels of a wide-band induction receiver compared to a system noise and a commercial (bigger size) induction coil.

The noise limiting factor for the next generation of AEM systems is likely to be the local ambient electromagnetic noise. In Figure 3.4 we have re-plotted the sensor noise spectra with the natural EM spectra at two field sites. The difference in the natural spectra is very large. The Richmond site is in an industrialized area near Berkeley and Joice Island is in a state park at least 10 miles from any built-up area. At 40 Hz the noise at Richmond is over 100 times that at Joice Island, and at 10^4 Hz they are about equal. The important point is that even in electromagnetically quiet areas the noise of the small coil is less than the ambient noise in the band of interest. There is no point of having sensors that are even less noisy since secondary fields from the target have to be detected in the presence of the ambient noise. Signal to noise enhancement is achieved by averaging or stacking of repeated transients, and so even if the sensor noise were equal to the ambient noise, the averaging time would only increase by a factor of $\sqrt{2}$.
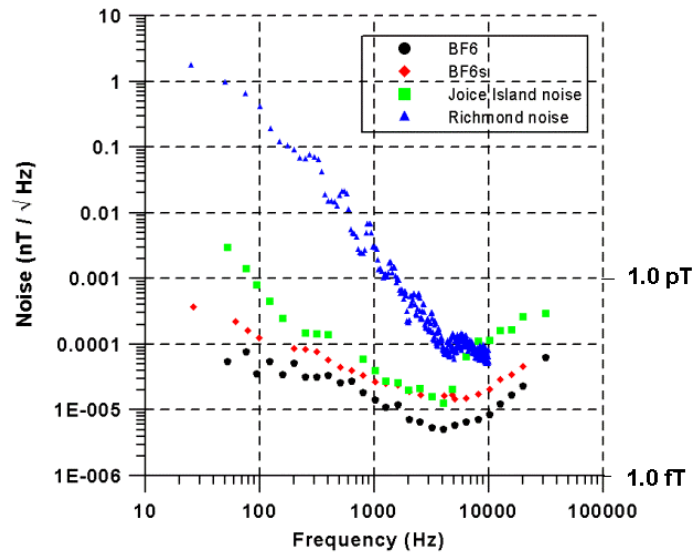
Figure 3.4: Noise levels of a wide-band induction receiver compared to the ambient noise at a quiet site near Berkeley, and at a noisy site.

EMI, Inc. has conducted many studies on the effects of length, diameter, and mass on the noise spectra of induction coils. Figure 3.5 is a summary of these studies. The figure shows noise level as a function of frequency for various sensor lengths. If the design goal were to have a sensor with a noise level of 1.0 pT at 100 Hz, and the ambient noise level at Joice Island, then from Figure 3.5 we see that it could be less than 10 cm in length. For 1.0 pT noise at 40 Hz it would need to be 10 cm long.
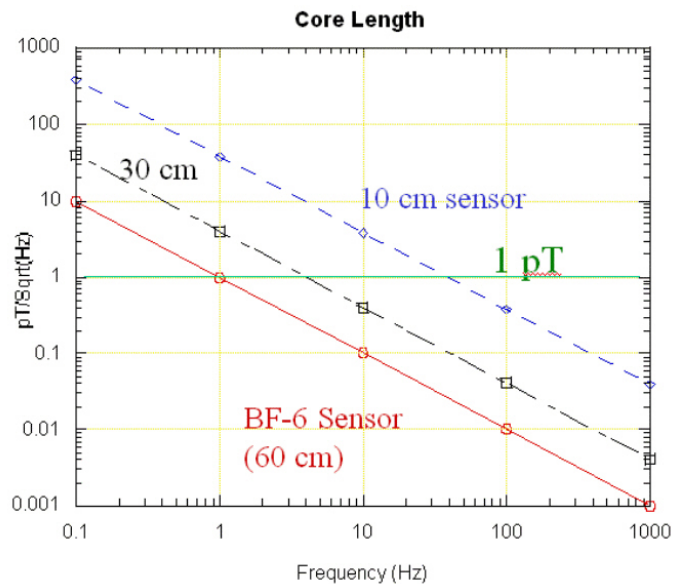
Figure 3.5: Noise level as a function of frequency for various sensor lengths.

Quasar, Inc. provided the noise spectra for the sensor shown in Figure 3.6. The sensor core length is 16.5 cm and noise level is about 200 fT (0.2 pT) at 100 Hz. This falls about exactly on the noise vs. length diagram of Figure 3.5, provided by EMI, Inc.
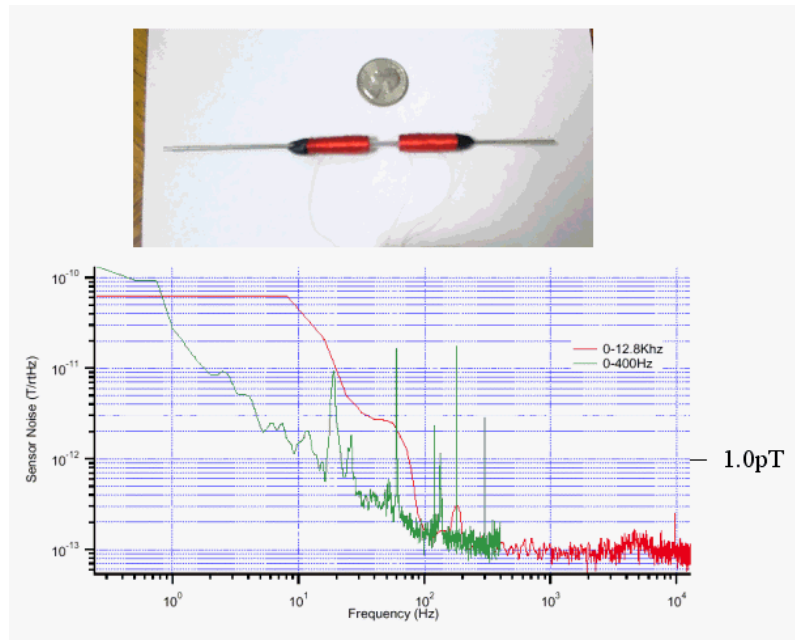
Figure 3.6: Quasar sensor.

The conclusion is that the small coils seem more than adequate for deployment in an array. In fact the size might be further reduced to simplify construction of the T-R system and reduce its weight.

4. BANDWIDTH REQUIREMENTS

The spectral and transient responses simulated in Section 2 were idealized responses that did not include the effects of the actual sensor response, discussed in Section 3, or very importantly the response of the amplifiers, filters, etc., which follow the sensor itself. Further the transient responses of Section 2 were for step function turn-off of the primary field. In practice square waves or other shaped repetitive waveforms are transmitted to enable stacking or averaging of the received secondary field wave forms to improve signal to noise ratio. The main impetus for working in the time (transient) domain is that only the secondary field exists after the primary field is turned off. The practical problem of identifying the secondary field in the presence of the primary field that exists in all frequency domain system is avoided. Unfortunately when the step function is replaced by a square wave such as that shown in Figure 4.1.1 the transient in the off-time is strongly influenced by the duration of the on-time of the pulse. The response in Figure 4.1.1 is that of the 37 mm solid magnetic sphere and the transients are shown in the off-times (T/4 to T/2, and 3T/4 to T, where T is the period of the square wave pattern) for varying T. The fundamental harmonic in the frequency representation of this waveform is 1/T, or in this case 860 Hz. This is below the frequency where the quadrature response peaks (solid magnetic sphere of Figure 2.3.4). As the period shortens the fundamental shifts higher and higher and vital low frequency characteristic of the response are lost. The transient plots in Figure 4.1.1 are somewhat misleading in that it appears that the longest period has the smallest transient. However if the off-time data are plotted as a function of time in seconds it would be seen that the long period transient was far larger than the shorter periods. This result is plotted quantitatively in Figure 4.1.2, where the mean square of the transient is plotted vs. period and it is seen that the maximum transient occurs at an optimum period Topt, which is in fact the inverse of the frequency at which the quadrature response for the solid magnetic sphere of Figure 2.3.4 peaks. This response is replotted here in Figure 4.1.3. Because we saw that lower frequencies are needed to better characterize the response, an operating frequency Fopr should be used even though the transient response will be less than optimum.
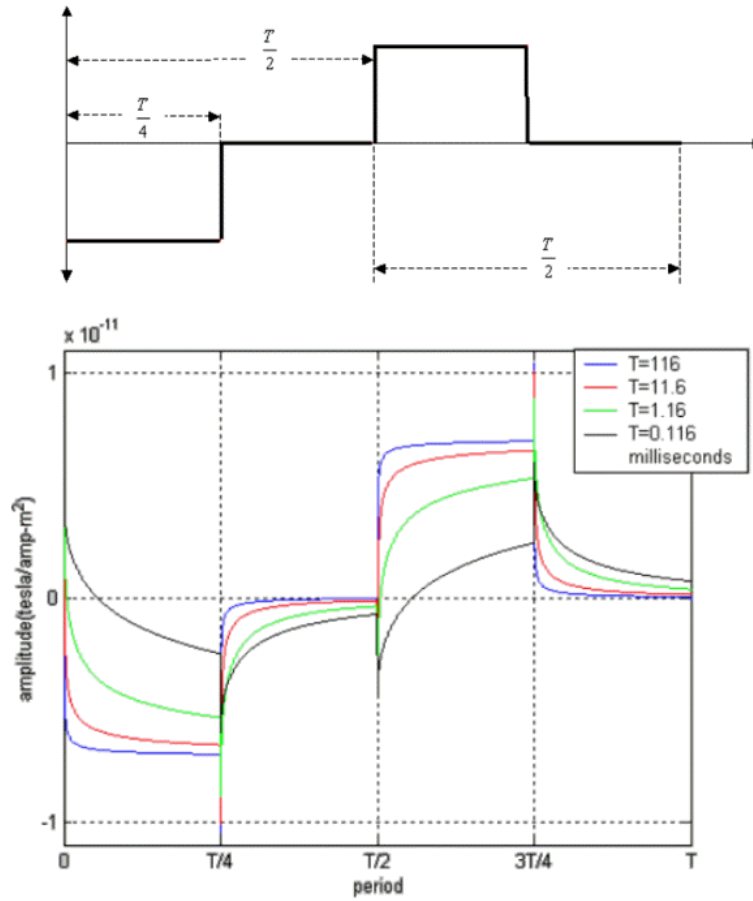
Figure 4.1.1: Transient response of 37 mm solid magnetic sphere in the off-times (T/4 to T/2, and 3T/4 to T) as a function of period T.
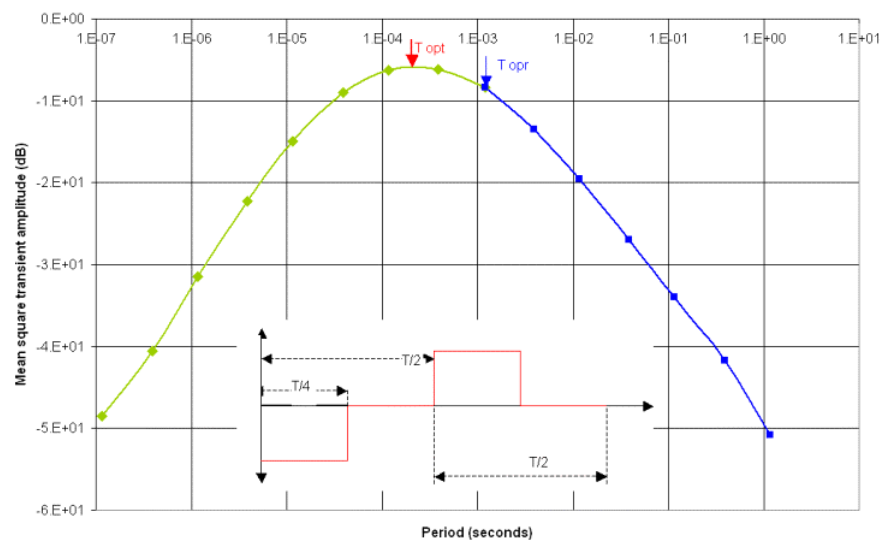
Figure 4.1.2: Mean square of the transient as function of period.
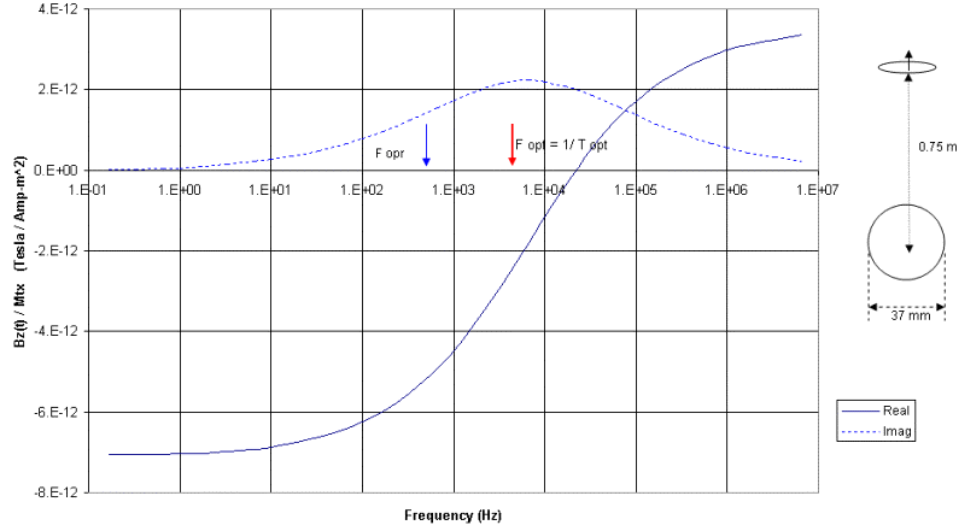
Figure 4.1.3: Normalized magnetic field response as a function of frequency for 37 mm magnetic sphere at 0.75 m depth plotted together with optimum (Fopt) and operating (Fopr) frequencies.

The ideal step function response is modified by the necessary choice of a repetitive square wave. This has the effect of reducing the transient and limits its frequency content. An interpretation of the data from any practical system must implicitly account for the source square wave period.

This example of the 37 mm magnetic sphere also serves to show the band limiting nature of the sensor itself and its role in further distorting or modifying the transient. In Figure 4.1.4 the frequency response of the 37 mm magnetic sphere is repeated with bandwidths of 40 Hz to 400 kHz, 400 Hz to 40 kHz, and 3.6 kHz to 4 kHz (the middle being the bandwidth of the BF-6s short sensor discussed in Section 3) indicated. The transients for the 1.16 msec square wave (fo = 860 Hz) are shown for the above two bandwidths and for a broadband system in Figure 4.1.5. Clearly the practical effect of the narrow band detector is to severely distort the transient while the broadband, 40 Hz to 400 kHz, appears to have very little effect at least on this linear scale. In detail however it can be seen in Figure 4.1.6 that the early time transient is severely distorted by the reduced bandwidth. This obviously will have a major impact on interpreting the subtle changes in transient response associated with different responses for the different polarizabilities of a body.
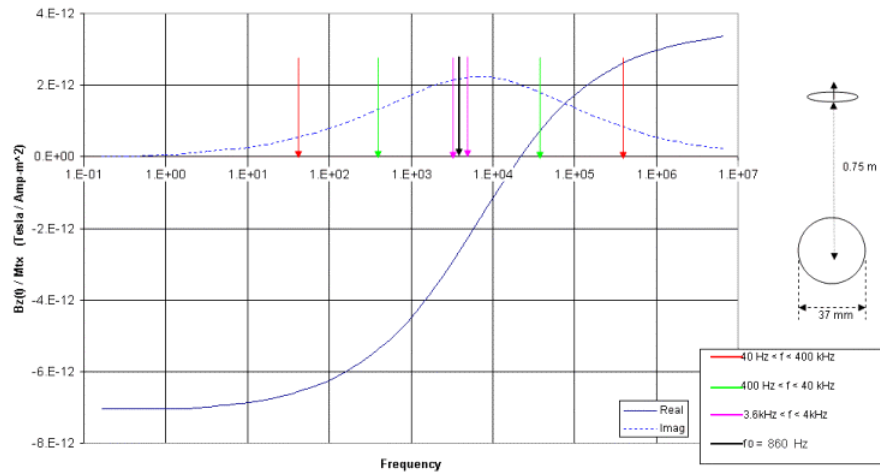
Figure 4.1.4: Normalized magnetic field response as a function of frequency for 37 mm magnetic sphere at 0.75 m depth plotted together with optimum (Fopt) and operating (Fopr) frequencies for several bandwidths.
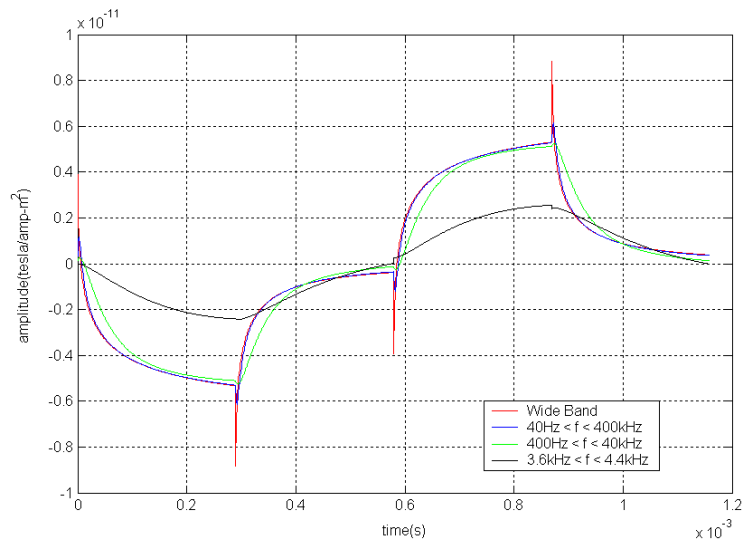
Figure 4.1.5: Effect of system bandwidth on the observable target signal (fo = 860 Hz).

43
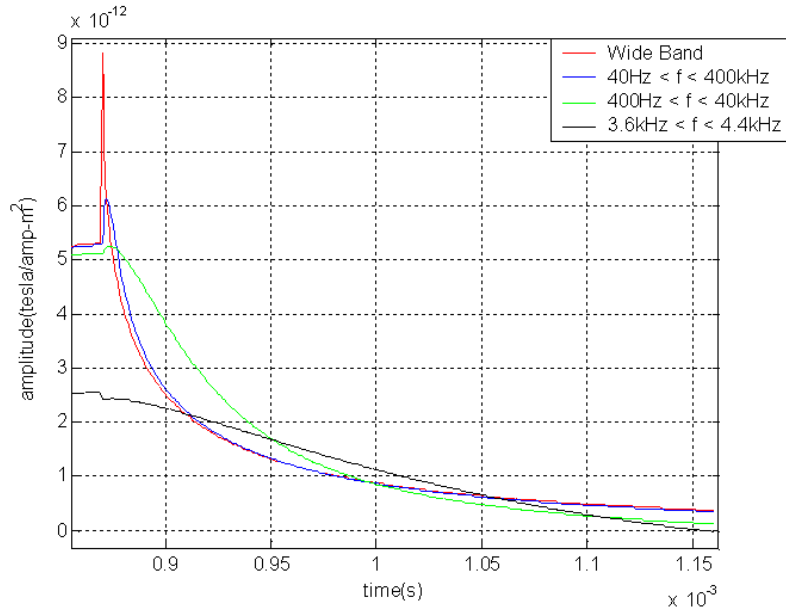
Figure 4.1.6: Effect of system bandwidth on the observable target signal (fo = 860 Hz) (detail).

In general the distortion introduced by the finite bandwidth of the sensor cannot be corrected by applying a system correction. The data outside the pass band is reduced below the system noise and deconvolution operations simply bring back unacceptable noise. Sensor bandwidth is reduced as much as possible, often using additional filtering in the following signal processing stages, to limit the noise but this carries the problem of distorting the transient response. Too narrow a band can distort the signal to the point where it is actually useless for detailed characterization of the target.

The feedback coil described in Section 3 is ideally suited for optimizing the bandwidth. Depending on circumstances, the sensor can be tuned and critically damped so that it shows the conventional dB/dt behavior. On the other hand, with the judicious use of feedback, the sensor can be made to have a flat response over many decades of frequency so that its behavior is more akin to that of magnetometer that measures B. In either case the dc target response cannot be recovered.

The idea for a sensor with wideband flat frequency response originated in France nearly forty years ago (Glerc and Gilbert, 1964). As shown below,
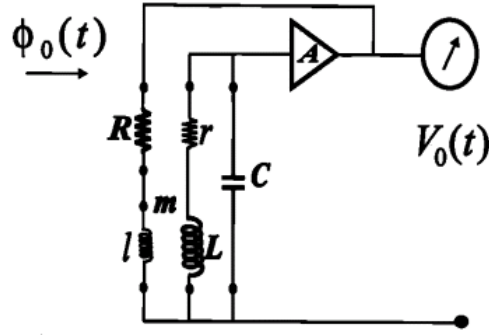
Figure 4.1.7: The wideband sensor.

This induction device consists of a principal winding denoted by its inductance "L" and resistance "r". It is tuned by the capacitance "C" to a central frequency "ω_0". The variable bandwidth feature is incorporated by feeding back the amplifier (gain A) output through a current limiting resistor R to an auxiliary winding, "l", which is inductively coupled to the principal winding by the mutual inductance "m". The receiver response is a function of the central frequency and the available feedback current. It is the latter that controls the system bandwidth as defined by the ratio of the highest to the lowest frequencies in the pass band, ω_H / ω_L. More precisely, $\omega_H / \omega_L = \omega_0 mA/2R = n^2$.

The frequency response for a variety of feedback settings as indicated by the parameter labels which correspond to values of ω_H / ω_L is shown below in Figure 4.1.8..
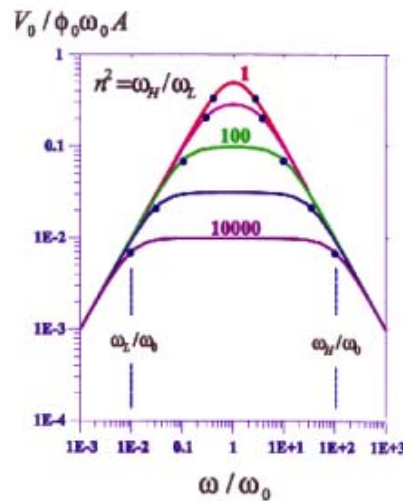
Figure 4.1.8: Frequency response of the wideband sensor.

Here we see how the sensor response varies, with the feedback parameter "n^2", as a function of the normalized frequency ω / ω_0. A feedback parameter value of unity corresponds to the classical critically damped induction receiver with no feedback. If ω_0, the resonant frequency of the receiver, is much greater than the frequency of peak target quadrature response then the sensor will in fact output a very close replica of the time derivative of the target signal. On the other hand, a sensor that is made to have a flat response over four decades of frequency by the application of massive feedback ($n^2 =$ 10,000), will in fact have an output voltage that is closely proportional to the actual secondary magnetic field generated by the target.

The discussion to this point has considered only the goal of recovery the B response. It is considerably easier to recover the true dB/dt response by moving the resonant frequency of the coil to a frequency much greater than the frequency of peak quadrature response and using a feedback parameter of unity. The low distortion recovery of dB/dt may offset the apparent disadvantages of using dB/dt that we discussed in Section 4. The main emphasis in the project at this stage is optimizing the sensor characteristics.

5. CONCLUSIONS AND ACCOMPLISHMENTS

A powerful simulator has been implemented for determining the optimum transmitter-receiver configuration for UXO detection and characterization. Another simulator has been developed for analyzing the role of bandwidth and noise in determining the spectral response of the principal dipole moments. From the simulators and from field measurements of ambient noise and the noise characteristics of a new compact magnetic field sensor, we have come to some preliminary conclusions about the requirements for an optimum AEM system. We have now begun a bench prototype development that will be used to test fabrication and measurement techniques and, with the simulator, will be used to optimize bandwidth, signal to noise ratio and transmitter power.

The major conclusions from research and development in calendar year 2002 are:

1) A multicomponent transmitter-receiver system is essential for the identification of the principal dipole moments of a target, be it UXO or clutter.

2) A three component loop transmitter with 5 small vector sensors suffices to uniquely determine the principal dipole moments of a target.

3) Similar detection/characterization results can be obtained, with different configurations, using deployment on a 2D grid, on a profile line, or in a stand alone mode.

4) The utility of grid or line deployment is limited by positioning accuracy.

5) For maximum utility a system capable of stand alone detection/characterization seems best because:

i) it can be used effectively when access does not permit precise line or grid operation.

ii) its sensitivity is independent of absolute position.

iii) when used in line or grid mode its sensitivity is superior to any other configuration.

6) Small, 10 to 15 cm long, sensors have been developed that are satisfactory for multiple receiver deployment within the footprint of the system (approx 1 m x 1m).

7) Feedback coils on the induction coil sensors permit them to be operated as field (B) detectors over a specified bandwidth or as dB/dt detectors over a specified bandwidth.

8) Simulation of the response of a range of elongated targets representative of UXO indicate that measurements of the magnetic field B may be more sensitive to target parameters than the time derivative, dB/dt.

9) The bandwidth of the receiver and its associated electronics have a profound effect on the secondary field transient and, in-turn, on the accurate recovery of the distinctive properties of the transient that enable the identification of the spectral properties of the target.

10) A bandwidth of at least four decades appears to be necessary to describe adequately the spectral response of the principal moments. Low frequencies are required to identify the permeability of the target and this in-turn requires a low pulse repetition rate for the transmitted fields.

11) The large bandwidth admits more noise and thus requires higher transmitter power to maintain an adequate signal to noise ratio.

6. REFERENCES

Barrow, B., Khadr, N., and Nelson, H.H., 1996, Performance of electromagnetic induction sensors for detecting and characterizing UXO: Proceedings of UXO Forum 1996, 308-314, Williamsburg, VA.

Baum, C. E., 1999, Low frequency near-field magnetic scattering from highly conducting, but not perfectly conducting bodies, in Baum, C. E., Ed., Detection and Identification of Visually Obscured Targets, Taylor and Francis, Philadelphia, 163-217.

Bell, T. H., Barrow, B., and Khadr, N., 1998, Shape-based classification and discrimination of subsurface objects using electromagnetic induction: IGARSS, Seattle, WA, July 6-10.

Clerc, G. and Gilbert,D, 1964. La Contre-reaction de Flux Appliquee aux Bobines a Noyau Magnetique: Annales de Geophysique, **20**, 499-502.

Keiswetter, D., Won, I.J., Barrow, B., and Bell, T.H., 1999, Object identification using multifrequency emi data: Proceedings of SAGEEP '99, 743-751, Oakland, March 14-18.

Khadr, N., Barrow, B. J., Bell, T. H., and Nelson, H. H., 1998, Target shape classification using electromagnetic induction sensor data: Proceedings of UXO Forum 1998.

McNeill, J.D., and Bosnar, M., 1996, Application of time domain electromagnetic techniques to UXO detection: Proceedings of UXO Forum 1996, Williamsburg, VA.

Morrison, H.F., Becker, A., Smith, J.M., Gasperikova, E., 2002. Detection and classification of buried metallic objects: EAGE Expanded Abstracts, Florence.

Pasion, L. R., and Oldenburg, D. W., 2001, Locating and determining dimensionality of UXOs using time domain electromagnetic fields: Journal of Environmental and Engineering Geophysics, **6**, 91-102.

Smith, J.T., and Morrison, H.F., 2002, Estimating equivalent dipole polarizabilities for the inductive response of isolated conductive bodies: IEEE Trans. Geosci. Remote Sensing, submitted for publication.

Smith, J.T., and Morrison, H.F., Becker, A., 2002, Depths of equivalent dipole polarizability resolution for some transmitter receiver configurations: IEEE Trans. Geosci. Remote Sensing, submitted for publication.

Smith, J.T., and Morrison, H.F., Becker, A., 2003, Optimizing receiver configurations for resolution of equivalent dipole polarizabilities in situ, in preparation.

Snyder, D.D., MacInnes, S., Urquhart, S., and Zonge, K.L., 1999, Possibilities for UXO classification using characteristic modes of the broad-band electromagnetic induction response: A New Technology Applications Conference on the Science and Technology of Unexploded Ordnance (UXO) Removal and Site Remediation, Outrigger Wailea Resort, Maui.

Ware, G.H., 2000, EM-63 data processing for UXO discrimination: Interim report, ESTCP, October 5.

Won, I.J., Keiswetter, D.A., Hanson, D.R., Novikova, E., and Hall, T.M., 1997, GEM-3: a monostatic broadband electromagnetic induction sensor: Journal of Environmental and Engineering Geophysics, **2**, 53-64.

7. LIST OF FIGURES